Quantifying the Snowfall Detection Performance of the GPM Microwave Imager Channels over Land

YALEI YOU AND NAI-YU WANG

Cooperative Institute for Climate and Satellites, Earth System Science Interdisciplinary Center, University of Maryland, College Park, College Park, Maryland

RALPH FERRARO AND SCOTT RUDLOSKY

NOAA/NESDIS/STAR, College Park, Maryland

(Manuscript received 6 August 2016, in final form 17 November 2016)

ABSTRACT

This study uses Global Precipitation Measurement (GPM) Microwave Imager (GMI) and Ka-precipitation radar observations to quantify the snowfall detection performance for different channel (frequency) combinations. Results showed that the low-frequency-channel set contains limited snow detection information with a 0.34 probability of detection (POD). Much better performance is evident using the high-frequency channels (i.e., POD = 0.74). In addition, if only one high-frequency channel is allowed to be added to the low-frequency-channel set, adding the 183 ± 3 GHz channel presents the largest POD improvement (from 0.34 to 0.50). However, this does not imply that the water vapor is the key information for snowfall detection. Only using the high-frequency water vapor channels showed poor snowfall detection with POD at 0.13. Further analysis of all 8191 possible GMI channel combinations showed that the 166-GHz channels are indispensable for any channel combination with POD greater than 0.70. This suggests that the scattering signature, not the water vapor effect, is essential for snowfall detection. Data analysis and model simulation support this explanation. Finally, the GPM constellation radiometers are grouped into six categories based on the channel availability and their snowfall detection capability is estimated, using channels available on GMI. It is found that type-4 radiometer (all channels) has the best snowfall detection performance with a POD of 0.77. The POD values are only slightly smaller for the type-3 radiometer (high-frequency channels) and type-5 radiometer (all channels except 183 channels).

1. Introduction

As the follow-on to the Tropical Rainfall Measuring Mission (TRMM), an objective of the Global Precipitation Measurement (GPM) mission is to detect falling snow (Hou et al. 2014; Skofronick-Jackson et al. 2015), which accounts for a significant fraction of precipitation occurrence in the middle and high latitudes (Mugnai et al. 2007; Liu 2008b; Kulie and Bennartz 2009; Behrangi et al. 2014). This study focuses on quantifying the snowfall detection performance of the GPM Microwave Imager (GMI).

Rainfall detection using passive microwave sensor over land has been researched extensively (Spencer et al. 1989; Grody 1991; Adler et al. 1994; Kummerow and Giglio 1994; Ferraro et al. 1994; Petty 1995; Kidd et al. 1998; Seto et al. 2005; Wang et al. 2009; Kacimi et al. 2013; Turk et al. 2014; You et al. 2015, 2016), whereas snowfall detection over land via passive microwave sensors is still at an early developmental stage. The brightness temperature (TB) depression at the high frequency (85 GHz) caused by the ice scattering generally is considered the primary signature for both rainfall and snowfall detection over land. Snowfall detection is more challenging than rainfall detection for several reasons. First, the snow accumulation on the ground in the cold season often presents a similar passive microwave signature as the falling snow (Grody 1991; Stephens and Kummerow 2007; Noh et al. 2009). The emissivity of the snow accumulation on the ground varies greatly depending on the snow wetness and snow grain microstructure (Mätzler 1994; Foster et al. 2012), making the surface emissivity difficult to model. Second, the nonspherical shape of ice particles and snowflakes

Corresponding author e-mail: Yalei You, yyou@umd.edu

DOI: 10.1175/JHM-D-16-0190.1

results in much more complex radiative properties than the approximately spherically shaped rain drops (Liu 2008a; Petty and Huang 2010). Third, the supercooled liquid water can increase the TB at high frequencies and obscure the TB depression signature caused by the scattering effect (Kulie et al. 2010; Löhnert et al. 2011; Xie et al. 2012; Liu and Seo 2013; Wang et al. 2013). Fourth, snowfall has a weaker scattering signature relative to rainfall (Skofronick-Jackson and Johnson 2011; Munchak and Skofronick-Jackson 2013; You et al. 2015). Therefore, the less-pronounced TB depression due to the weaker scattering is more easily obscured by other signals (e.g., surface contamination and supercooled liquid water).

Despite these challenges, several sensitivity studies have shown promising results for snowfall detection over land using high-frequency microwave channels. Theoretical radiative transfer modeling studies have shown that frequencies around 150 GHz are probably most appropriate for snowfall detection in the middle and high latitudes (Bennartz and Bauer 2003). They also noted that channels near 85 and 183 ± 7 GHz showed potential for snow detection. Di Michele and Bauer (2006) also found that the high frequencies (95–100, 140–150, and 187 GHz) are most suitable for snowfall retrieval over land. Case studies using radiative transfer models and the Weather Research and Forecasting (WRF) Model showed that the 166-GHz TB provides the best detection capability for falling snow over land, and that low frequencies (<89 GHz) contain very weak falling snow signals (Skofronick-Jackson et al. 2013). Foster et al. (2012) analyzed a snowfall case over the mid-Atlantic region of the United States using satellite- and ground-based radar measurements. They found a clear TB depression tendency in the high-frequency channels from the Advanced Microwave Sounding Unit-B (AMSU-B) and Microwave Humidity Sounder (MHS). Similar results (i.e., high-frequency channels containing snowfall detection information) have also been found over ocean (Liu and Curry 1997; Katsumata et al. 2000).

Several snowfall detection algorithms have been developed over land. Previous studies were able to delineate the possible snowfall regions using the TBs at the opaque oxygen band channel (54 GHz) and water vapor band channel (183 GHz) from AMSU-B (Staelin and Chen 2000; Chen and Staelin 2003; Surussavadee and Staelin 2009). It is shown that the snowfall regions detected by the TBs are roughly consistent with the ground-based radar for a snowfall event over the New England region of the United States. The authors also demonstrated that the TBs are able to capture the major features of the snowfall events over the Arctic region, by comparing with the *CloudSat* observations. Kongoli et al. (2003) presented a threshold technique for snow detection that uses coincident ground station snow observations and TBs from AMSU-B. The threshold technique identifies the possible snowfall regions by assigning several threshold values for TBs at different channels (e.g., 183 ± 3 GHz). The primary channels include 150, 183 ± 1, 183 ± 3, and 183 ± 7 GHz. The 53.6-GHz TB is used to filter out the possible cold snow observations (i.e., snowfall with surface air temperatures colder than −6°C). Case studies showed that the snowfall identification agrees well with ground-based radar observations. This framework recently has been extended to the Advanced Technology Microwave Sounder (ATMS) for both warm and cold weather conditions (Kongoli et al. 2015). It is found that better snowfall detection performance occurs during the relatively warmer weather conditions with average surface temperature of about −3.1°C due to the larger scattering effect. Liu and Seo (2013) created a lookup table for snowfall detection using three leading principal components of TBs at high frequencies (from 89 to 183 ± 7 GHz) from AMSU and MHS data. They noted that the retrieved snow probability agrees well with *CloudSat* radar observations. In contrast to the aforementioned studies, which almost exclusively use the TBs at high-frequency channels, Turk et al. (2014) proposed a linear discriminant analysis technique that condenses all frequency channels (both low and high) into one single pseudochannel. This method has been successfully applied to Special Sensor Microwave Imager/Sounder (SSMIS) and ATMS for snowfall detection by You et al. (2015) and (2016).

The statistical snowfall detection methods are complemented by physical snowfall detection models. Skofronick-Jackson et al. (2004) presented a physical model for snowfall detection that leverages both radiative transfer and mesoscale cloud models. The snow microphysical parameters are derived from the mesoscale model (i.e., temperature, relative humidity profiles, and the vertical distribution of hydrometeors). This physical model was able to capture the major features of a blizzard in the United States. Kim et al. (2008) improved this model by calculating the scattering properties more precisely and using more realistic snow particle size distributions. Noh et al. (2009) developed a Bayesian framework for snowfall detection and retrieval using the high-frequency microwave observations (>85 GHz). They used ground and spaceborne radar observations along with WRF Model outputs to simulate TB. This algorithm is applied to the AMSU-B observations over the Great Lakes region. It is shown that the detection and retrieval results agree well with the

TABLE 1. GPM constellation radiometers grouped into six types based on channel availability for the different radiometer types. The sensors that employed the cross-track scanning scheme are indicated with an asterisk. Other sensors use the conical scanning scheme. For the cross-track scanning sensors, the polarization (V/H) is valid only at nadir. All values in Table 1 are rounded to one digit. However, throughout the text, the number is rounded into an integer for simplicity.

	6–7 GHz	10 GHz	19 GHz	23 GHz	31–37 GHz	50–60 GHz	80–92 GHz	150–167 GHz	183–190 GHz
1: Low-frequency channels									
WindSat	6.8 V/H	10.7 V/H	18.7 V/H	23.8 V/H	37.0 V/H				
TMI		10.7 V/H	19.4 V/H	21.3 V	37.0 V/H		85.5 V/H		
AMSR-E	6.9 V/H	10.7 V/H	18.7 V/H	23.8 V/H	36.5 V/H		89.0 V/H		
2: Low-frequency channels + 89 GHz									
AMSR2	6.9/7.3 V/H	10.7 V/H	18.7 V/H	23.8 V/H	36.5 V/H		89.0 V/H		
AMSU-A*				23.8 V	31.4 V	50.3–57.3 V/H	89.0 V		
SSMI			19.4 V/H	22.2 V	37.0 V/H		85.5 V/H		
3: High-frequency channels									
AMSU-B*							89.0 V	150.0 V	183.3 V
MHS*							89.0 V	157.0 V	183.3 H /190.3 V
SSMIS			19.4 V/H	22.2 V	37.0 V/H	50.3–63.3 V/H	91.7 V/H	150.0 V	183.3 H
4: All channels									
GMI		10.7 V/H	18.7 V/H	23.8 V	36.5 V/H		89.0 V/H	166.0 V/H	183.3 V/H
ATMS*				23.8 V	31.4 V	50.3–57.3 V/H	88.2 V	165.5 H	183.3 H
5: All except 183-GHz channels									
MADRAS			18.7 V/H	23.8 V	36.5 V/H		89.0 V/H	157 V/H	
6: 183-GHz channels									
SAPHIR*									183.3 H

surface radar observations when there is little snow accumulation on the ground. However, larger false detection and overestimated snowfall rates occur during the late winter because of the frequent snow cover on the ground.

Previous sensitivity experiments and algorithm development have clearly demonstrated that high-frequency TB (>85 GHz) can be used to detect falling snow. However, several questions remain:

1) How much information do the low-frequency channels contain for snowfall detection over land?
2) How important are the high-frequency channels for snow detection?
3) What is the optimal channel combination for snowfall detection?

Observations from the GPM are explored to quantify the channel importance and address these important questions. Another objective of this study also seeks to quantify the snowfall detection capability of the 13 GPM constellation radiometers (see Table 1; more details are provided in section 6).

This paper is organized as follows. A brief overview of the datasets used in this work is provided in section 2. The statistical method for snowfall detection is presented in section 3. Section 4 quantifies the low- and high-frequency channels' detection capability for snowfall detection. Section 5 demonstrates the snowfall detection skills by all possible channel combinations from these 13 GMI channels. The snowfall detection performance for GPM constellation radiometers estimated by GMI is shown in section 6. Section 7 summarizes the results and discusses implications of this work.

2. Data

The primary data used in this study are the snowfall observations from Ka-band precipitation radar (KaPR; 35.5 GHz; Seto et al. 2013) and TBs from GMI (Draper et al. 2015). This study uses data from March 2014 through December 2015 over land regions between 65°S and 65°N.

The swath width of KaPR is 120 km and the footprint size is 5 km at nadir. Vertically, the KaPR is able to detect precipitation from 0 to 20 km at a 250-m resolution. There are four versions of the KaPR-retrieved precipitation rate, depending on different measurements and ancillary data used in the retrieval process. These include the Ka level-2A product (2AKa), Ka level-2A product with atmospheric state environmental information (2AKaENV), Dual-Frequency Precipitation Radar (DPR) level-2A product (2ADPR), and DPR level-2A product with atmospheric state environmental information (2ADPRENV). In this study, we use the snowfall data from the 2ADPR high-sensitivity (HS) scans (Hamada and Takayabu 2016). In this product, both KaPR and Ku-band precipitation radar (KuPR) measurements are used to estimate the precipitation rate, which theoretically is more accurate than the estimate from either single-frequency radar.

To avoid the sidelobe contamination, only observations from the central 16 scan lines (bin 5–20 for KaPR) are used.

The GMI sensor is a conical-scan passive microwave radiometer, which has 13 frequencies ranging from 10.65 to 183.3 GHz, including 10.7 (V/H), 18.7 (V/H), 23.8 (V), 37.0 (V/H), 89.0 (V/H), 166.0 (V/H), 183.3 ± 3 (V), and 183.3 ± 7 (V) GHz (for vertical V and horizontal H polarizations). These frequencies (or part of them) are widely available on other GPM constellation passive microwave radiometer sensors. Hereafter, these channels will be referred to as V10, H10, …, V183 ± 7 for convenience. Also, we will refer to the frequency as 10, 19, 24, 37, 89, 166, 183 ± 3, and 183 ± 7 GHz for simplicity.

The hourly column-integrated total water vapor (TWV) at approximately 0.5° resolution is from the Modern-Era Retrospective Analysis for Research and Applications (MERRA) dataset (Rienecker et al. 2011). Surface snowfall observations from the National Climatic Data Center (NCDC) Integrated Surface Database (ISD) are used as the surface reference (Smith et al. 2011).

The spatial resolutions among GMI channels vary from 19 km × 32 km at 10 GHz to 4 km × 5 km at 183 ± 7 GHz (Draper et al. 2015). Data collocation was performed to analyze coincident data from all of these channels. First, the resolution at V37 (8.6 km × 14.4 km) is taken as the nominal resolution. The four closest pixels at higher frequencies from 89 to 183 ± 7 GHz are chosen, and then the TBs from these four pixels are averaged by different weights to represent the corresponding TBs at the nominal resolution. The weights are calculated by the function $\exp(-r^2/2\sigma^2)$, where r is the distance and σ is a constant that is determined by letting the weight reduce to one-half when r increases from zero to one-half of the effective field of view (FOV) of the 37 GHz. The effective FOV of the 37 GHz is 12 km (Draper et al. 2015). The present study uses the lower-frequency channels (i.e., 10, 19, and 24 GHz) at their native spatial resolution. This collocation procedure is similar to Fu and Liu (2001). For each collocated GMI pixel, the pixel is deemed as a snow pixel if the snowfall rate from any of the closest four KaPR pixels is greater than 0 mm h^{-1}. Otherwise, the pixel is taken as a no-snow pixel.

For TWV, we use the data from the closest grid to match the 37-GHz pixel resolution. In addition, the TWV observations are linearly interpolated to match the time of the TB observation. Specifically, we first find the nearest grid box to the collocated GMI pixel by calculating the distance between each grid box and the pixel central latitude–longitude. Then the 24 TWV values in the corresponding grid are linearly interpolated to match the time of the GMI pixel.

The authors again emphasize that in the present study the low-frequency channels always indicate that the channel central frequency is less than 85 GHz (e.g., 10, 19, 24, and 37 GHz), while the high-frequency channels represent those with central frequency greater than or equal to 85 GHz. (e.g., 85, 166, and 183 GHz). This definition for high- and low-frequency channels is widely accepted in the precipitation retrieval and validation community (e.g., Ferraro et al. 1994; Wang et al. 2009; Kummerow et al. 2011; Skofronick-Jackson and Johnson 2011; You et al. 2011; You and Liu 2012; You et al. 2014).

3. Methodology

This study detects snowfall using a linear discriminant analysis (LDA) approach. The LDA approach condenses multiple variables into a single variable while retaining as much discriminatory information as possible. In terms of snowfall detection, we construct two databases (snow and no-snow) based on KaPR observations that contain multivariables **x** (TBs). According to Wilks (2011), the linear discriminant function to distinguish these two groups is

$$\delta_1 = \mathbf{a}^{\mathrm{T}} \times \mathbf{x}, \tag{1}$$

where T stands for the transpose and **a** is the discriminant vector, calculated in the following way:

$$\mathbf{a} = \mathbf{S}_{\mathrm{pool}}^{-1}(\overline{\mathbf{x}}_1 - \overline{\mathbf{x}}_2) \quad \text{and}$$
$$\mathbf{S}_{\mathrm{pool}} = \frac{n_1 - 1}{n_1 + n_2 - 2}\mathbf{S}_1 + \frac{n_2 - 1}{n_1 + n_2 - 2}\mathbf{S}_2, \tag{2}$$

where $\overline{\mathbf{x}}_i$ and $\mathbf{S}_i$ ($i = 1, 2$) represent the mean vector and covariance of each group, respectively, and $\mathbf{S}_{\mathrm{pool}}$ is the weighted average of the two sample covariance matrices from these two datasets. The boldface variables represent vectors. Variables n_1 and n_2 are the samples size in these two groups, respectively.

A decision to classify an observation **x** as a snow or no-snow pixel can be made according to the value of the scalar δ_1. Previous work (Turk et al. 2014; You et al. 2015, 2016) showed that the LDA method performs well for rainfall and snowfall detection. Similar to the widely use scattering index (Grody 1991), the δ_1 is named as discrimination index (DI).

The probability of detection (POD) [Eq. (3)] was selected to evaluate snowfall detection performance using different channel combinations. Larger POD values indicate better snowfall detection. To conduct a meaningful and fair comparison between different PODs from different channel combinations, the false alarm

TABLE 2. Notation for snow/no-snow results judged by KaPR and GMI.

	Snow judged by KaPR	No snow judged by KaPR
Snow judged by GMI	*a*	*b*
No snow judged by GMI	*c*	*d*

rate (FAR) must be fixed since POD and FAR are inherently related. In the current work, the FAR is fixed at 0.10. Choosing other FAR threshold values (e.g., 0.05 and 0.15) will change the numerical values of POD but the conclusions hold. POD and FAR are defined by the following equations:

$$\mathrm{POD} = \frac{a}{a+c} \quad \text{and}$$
$$\mathrm{FAR} = \frac{b}{b+d}, \tag{3}$$

where the definitions for a, b, c, and d are given in Table 2.

4. Sensitivity experiments of different channel combinations

a. *Snow detection performance of low-frequency channels*

In this section, the snow detection performance from low-frequency channels is quantified using actual GPM observations.

Figure 1 provides a demonstration of the LDA detection approach by showing the histograms for snow and no-snow scenarios derived from the all-low-frequency-channel combination (V10, H10, V19, H19, V24, V37, and H37) and the all-high-frequency-channel combination (V89, H89, V166, H166, V183 ± 3, and V183 ± 7). The snow and no-snow histograms largely overlap each other for the low-frequency-channel set (Fig. 1a). This demonstrates very limited separation information from the low-frequency channels. In contrast, the snow and no-snow curves show much better separation using the all-high-frequency-channel set (Fig. 1b). Quantitatively, the POD from the all-low-frequency-channel set is only 0.34, while the POD is 0.74 from the all-high-frequency-channel set (Fig. 2; corresponding to the FAR at 0.10; green dashed line).

As mentioned previously, we choose the POD value corresponding to FAR at 0.1 to judge the snowfall detection performance for different channel or channel combinations. Selecting other FAR values does not change the conclusions. For example, the POD values for low-frequency channels and all high-frequency channels are 0.34 and 0.74, corresponding to FAR at 0.10 (vertical green dashed line). Corresponding to FAR at 0.05 (vertical black dashed line), they are approximately 0.2 and 0.6 (see Fig. 2), respectively.

We next calculate the PODs from all possible combinations of the low-frequency channels [(V10 and H10), (V10, V19, and H37), etc.]. There are 127 possible low-frequency-channel combinations out of these seven low-frequency channels ($C_7^1 + C_7^2 + \ldots + C_7^7 = 127$). Variable C_7^k stands for the number of combinations by selecting k channels from seven low-frequency channels, where k is from 1 to 7.

Figure 3 shows the histogram of these POD values. For example, there are 26 of these low-frequency-channel combinations with POD values around 0.25.

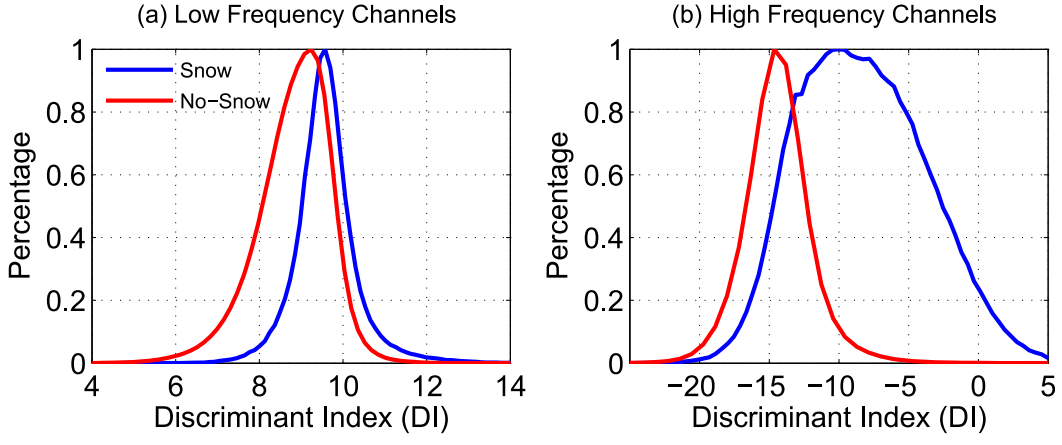

FIG. 1. (a) Histograms of the DI derived from the all-low-frequency-channel combination (V10, H10, V19, H19, V24, V37, and H37) for snow and no-snow scenes. Both histograms have been scaled by the corresponding max value in each histogram. (b) As in (a), but for the all-high-frequency-channel combination (V89, H89, V166, H166, V183 ± 3, and V183 ± 7).

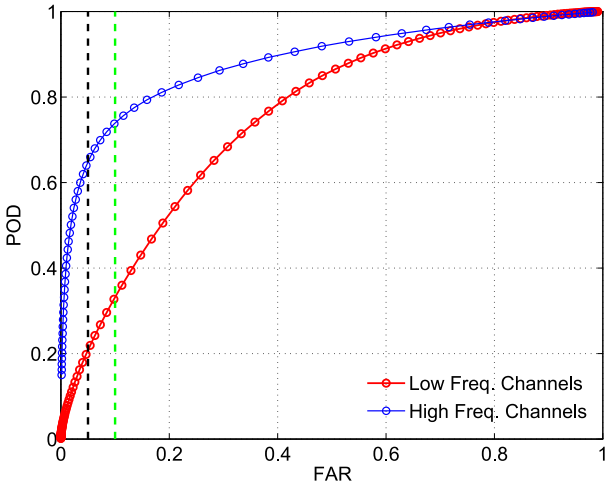

FIG. 2. POD vs FAR at different DI thresholds for the all-low-frequency-channel combination (V10, H10, V19, H19, V24, V37, and H37) and the all-high-frequency-channel combination (V89, H89, V166, H166, V183 ± 3, and V183 ± 7). The green dashed line stands for the FAR at 0.10.

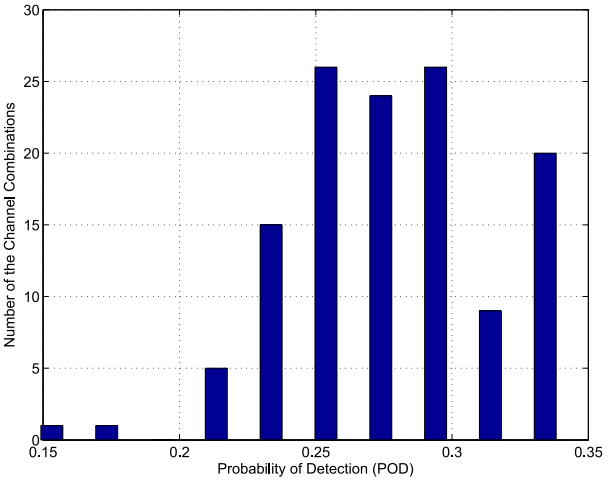

FIG. 3. Histogram of the PODs derived from 127 possible all-low-frequency-channel combinations.

The small POD values clearly show poor snow detection capability for low-frequency channels, regardless of the low-frequency channel or channel combinations. The best POD from these low-frequency-channel combinations is 0.34.

Figure 4 further demonstrates the snowfall detection capability of the low-frequency channels by three snowfall events on 6 January 2015 over the U.S. Great Lakes region, on 28 January 2015 over eastern China, and on 17 January 2015 over Siberia, Russia. The all-low-frequency-channel combination (V10, H10, V19, H19, V24, V37, and H37) is used in the case studies because it is one of the combinations associated with the largest POD (0.34; Fig. 3).

The low-frequency-channel set almost completely missed the snowfall occurrence for the Great Lakes snow event, as indicated by ground station observations (magenta cross in Figs. 4a–c), KuPR (green dots in Fig. 4b), and KaPR (red dots in Fig. 4c). Conversely, the low-frequency channels falsely indicate snowfall occurrence in the southern portion of the swath, where KuPR, KaPR, and ground stations observe no snowfall. The low-frequency-channel set does capture most of the snowfall occurrence for the snowfall event over eastern China. However, false detections north of 45°N and in areas around Beijing are also evident, since the ground station reports no snowfall. The dense ground-station observation network around Beijing makes it highly unlikely that they all missed snowfall if snowfall indeed occurred. Similar to the snowfall event over eastern China, false snowfall detections are apparent south of 50°N for the snowfall case in Siberia, Russia, where ground stations, KuPR, and KaPR detect no snowfall.

The snowfall occurrence frequency is calculated for each 1° grid box in the GPM coverage area (65°S–65°N) from December 2014 to February 2015 (Fig. 5). The frequency is the snowfall occurrence count divided by the count of all observations in each grid box, as indicated either by KaPR (Fig. 5a) or the low-frequency-channel set (Fig. 5b). Overall, the snowfall frequency pattern derived from low-frequency-channel set is opposite to that from KaPR. That is, the occurrence frequency from the low-frequency-channel set is smaller in the high-latitude regions (north of 45°N) and larger in the low-latitude regions relative to the KaPR observations. The low-frequency-channel set misses many snowfall events in Alaska, northeastern Canada, western Russia, and the Kamchatka Peninsula. Low frequencies also underestimate the snowfall occurrence frequency over Japan. Conversely, in relatively low latitudes (e.g., southwestern United States and areas from the Black Sea to the Caspian Sea), the snowfall frequency is much larger than that from KaPR. Note that the snowfall frequency pattern derived from KaPR is roughly consistent with that derived from the 94-GHz *CloudSat* cloud profiling radar (Liu 2008b; Behrangi et al. 2014; Kulie et al. 2016).

In summary, this section demonstrates the limited snowfall detection capability from the low-frequency channels. Regardless of the low-frequency channel or channel combination, the largest POD is 0.34. These findings support many previous theoretical studies (Bennartz and Bauer 2003; Di Michele and Bauer 2006; Skofronick-Jackson et al. 2004). Relative to the high-frequency channels, the less sensitivity to the ice-scattering

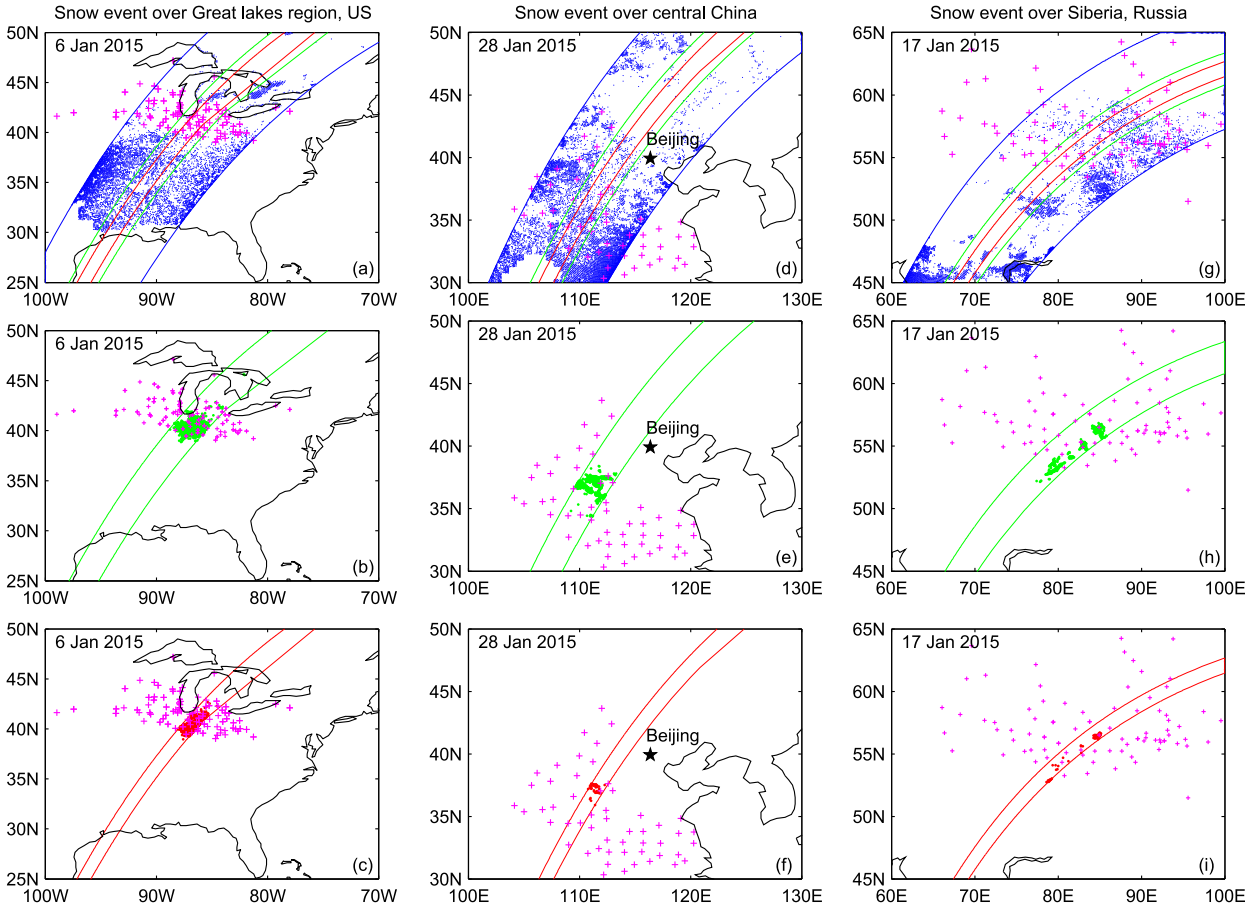

FIG. 4. (a) Snow detection performance of the all-low-frequency-channel combination (V10, H10, V19, H19, V24, V37, and H37; type-1 radiometer; see Table 1) for a snow event over the Great Lakes region on 6 Jan 2015. Blue, green, and red curves represent the GMI, KuPR, and KaPR swath boundaries, respectively. Blue dots represent the snow occurrence derived from the low-frequency channels. (b) Snowfall occurrence observed by KuPR (green dots). (c) Snowfall occurrence observed by KaPR (red dots). (d)–(f) As in (a)–(c), but for the snow event over eastern China on 28 Jan 2015. (g)–(i) As in (a)–(c), but for the snow event over Siberia, Russia, on 17 Jan 2015. The magenta plus signs represent the snowfall occurrence reported by the ground observations.

signal of the low-frequency channel and the larger surface contamination are largely responsible for the poor snowfall detection performance of the low-frequency channels. The larger FOV of the low-frequency channels may also contribute to the poor snowfall detection performance.

b. Importance of the high-frequency channels

1) POD IMPROVEMENT BY ADDING HIGH-FREQUENCY CHANNELS

The previous section demonstrates the limited snowfall detection information provided by the low-frequency channels. This section will illustrate the importance of high-frequency channels for snowfall detection. To this end, the POD calculated from the low-frequency-channel set (V10, H10, V19, H19, V24, V37, and H37) provides the benchmark. The high-frequency channels (V89, H89, V166, H166, V183 ± 3, and V183 ± 7) are then added one by one to determine how much POD improvement can be achieved by adding one high-frequency channel to this low-frequency-channel set.

Figure 6 showed the PODs from the low-frequency-channel set and low-frequency-channel set plus one single high-frequency channel. The POD based only on the low-frequency channel set is 0.34. The POD is almost identical after adding the V89 or H89 channel, which is probably because this channel is still highly influenced by the surface conditions in the snowfall scenarios due to the weak snowfall-scattering signature. The POD increases to 0.43 and 0.46 by adding the V166 and H166 channels to the low-frequency-channel set, respectively. The POD increases to 0.46 when adding the V183 ± 7 channel. The greatest improvement results

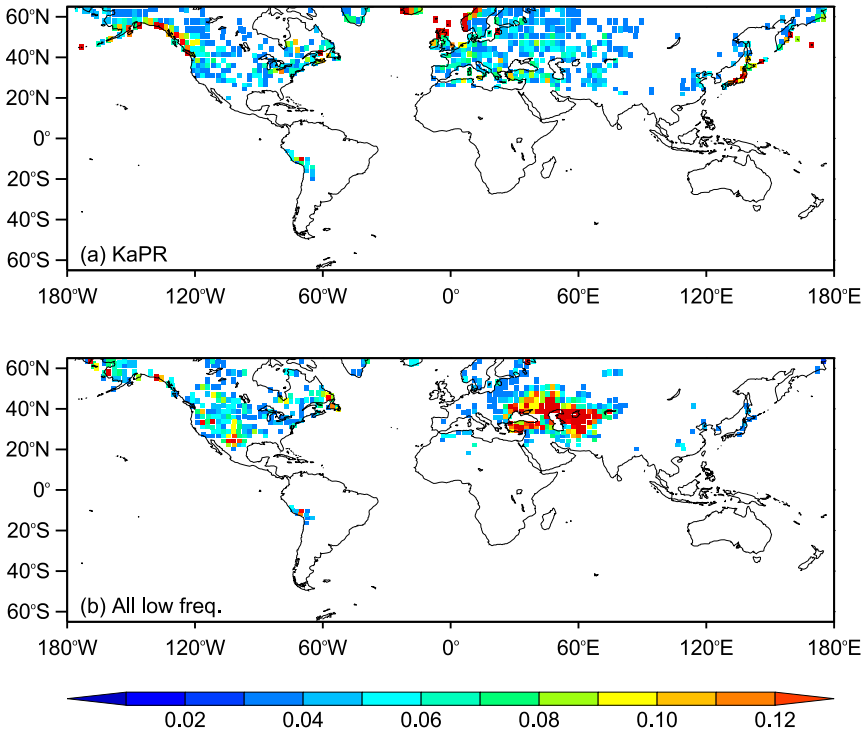

FIG. 5. Geospatial distribution of the snowfall occurrence frequency from December 2014 to February 2015 derived from (a) KaPR and (b) the all-low-frequency-channel combination (V10, H10, V19, H19, V24, V37, and H37).

from adding the V183 ± 3 water vapor channel to the low-frequency-channel set (POD increases to 0.50). This result is somewhat surprising since previous model simulations (e.g., Bennartz and Bauer 2003; Skofronick-Jackson et al. 2013; Shi et al. 2010) have shown that the high-frequency window channel (e.g., 166 GHz) is the more sensitive channel for snowfall detection over land (due to the large scattering signal) than the water vapor channels (e.g., V183 ± 3). However, our observation-based analysis shows that adding the V183 ± 3 water vapor channel to the low-frequency-channel set provides greater snowfall detection improvement than adding the V166 channel. To better understand this finding, the PODs from several channel combinations are calculated (next section), conditioned on TWV and snowfall rate. The snowfall rate throughout this study is the water equivalent.

2) POD UNDER DIFFERENT TWV AND SNOWFALL INTENSITY SCENARIOS

We next explore why adding the V183 ± 3 channel to the low-frequency-channel set improves the POD most. The PODs from the low-frequency channel set (V10, H10, …, and H37), low-frequency-channel set plus V166 (V10, H10, …, H37, and V166), low-frequency-channel set plus V183 ± 3 (V10, H10, …, H37, and V183 ± 3), and low-frequency-channel set plus V183 ± 7 (V10, H10, …, H37, and V183 ± 7) are calculated under different TWV and snowfall rate situations (Fig. 7).

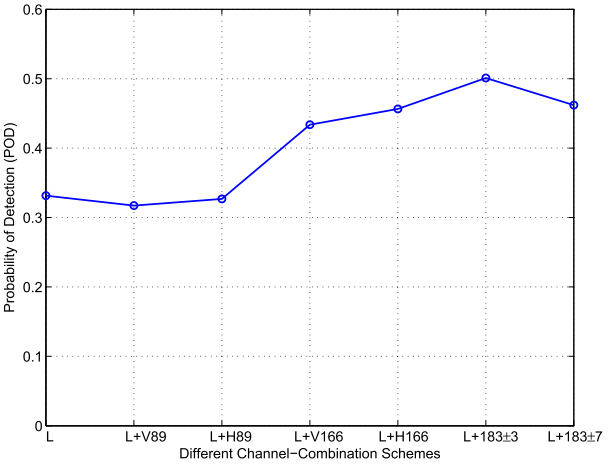

FIG. 6. POD derived from the all-low-frequency-channel combination (V10, H10, V19, H19, V24, V37, and H37) (denoted by letter *L* in the *x*-axis label) and the all-low-frequency-channel combination plus one single high frequency (V89, H89, V166, H166, V183 ± 3, and V183 ± 7).

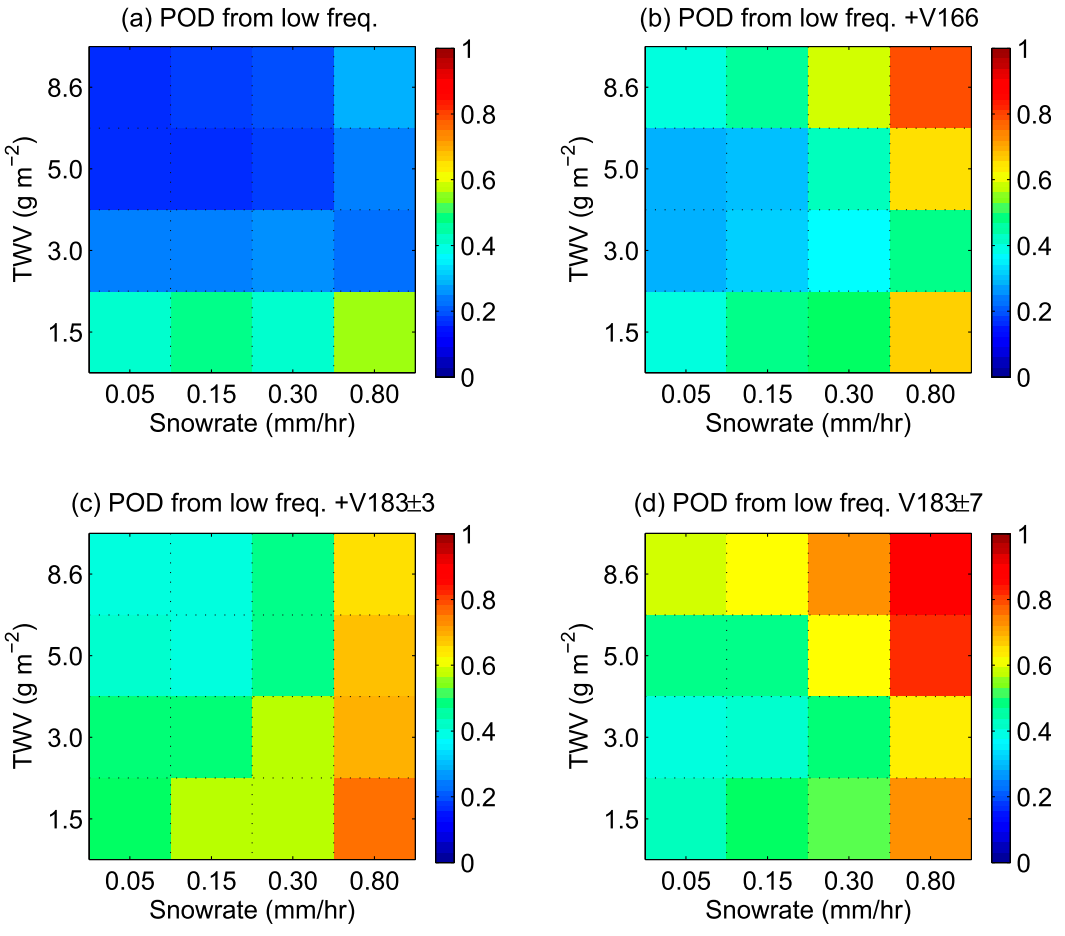

FIG. 7. Under different water vapor and snowfall intensity scenarios, (a) POD derived from the all-low-frequency-channel combination (V10, H10, V19, H19, V24, V37, and H37), (b) POD derived from the all-low-frequency-channel combination plus the V166 channel, (c) POD derived from the all-low-frequency-channel combination plus the V183 ± 3 channel, and (d) POD derived from the all-low-frequency-channel combination plus the V183 ± 7 channel.

Both TWV and snowfall rate are divided into four categories with boundaries corresponding to the 25%, 50%, and 75% values of each variable. The snowfall rate is derived from KaPR reflectivity observations.

Adding the V166, V183 ± 3, and V183 ± 7 channels to the low-frequency-channel set improves the POD, regardless of the snowfall intensity and water vapor environment (Fig. 7). To quantify this improvement, the POD values from the low-frequency-channel set are differenced with those from the low-frequency-channel set plus V166, V183 ± 3, and V183 ± 7 (Fig. 8). Adding these channels to the low-frequency-channel set clearly increases the PODs, as indicated by the positive differences in Figs. 8a–c. However, the degree of improvement varies considerably under different conditions. For example, adding the V183 ± 3 channel to the low-frequency-channel set improves the POD more than adding the V166 channel, except when the TWV is around 8.6 g m^{-2} (cf. Figs. 8a,b). With TWV less than 5.0 g m^{-2}, greater POD improvement is observed by adding the V183 ± 3 channel than adding the V183 ± 7 channel (cf. Figs. 8a,c). The vast majority (96.9%) of the total pixels are in the categories with TWV less than 5.0 g m^{-2} (Fig. 8d). Mathematically, this explains why adding the V183 ± 3 channel produces the largest overall POD improvement when using all pixels to calculate POD.

We have also analyzed the POD difference between low-frequency channels and low-frequency channels plus 89 GHz (not shown). It appears that by adding 89 GHz the POD changes very little, except that the POD increases about 0.10 and 0.13 under moist winter environments (TWV at about 8.6 g m^{-2}) and heavy snowfall (0.30 and 0.80 mm h^{-1}), respectively. The relatively large scattering signature leads to the POD

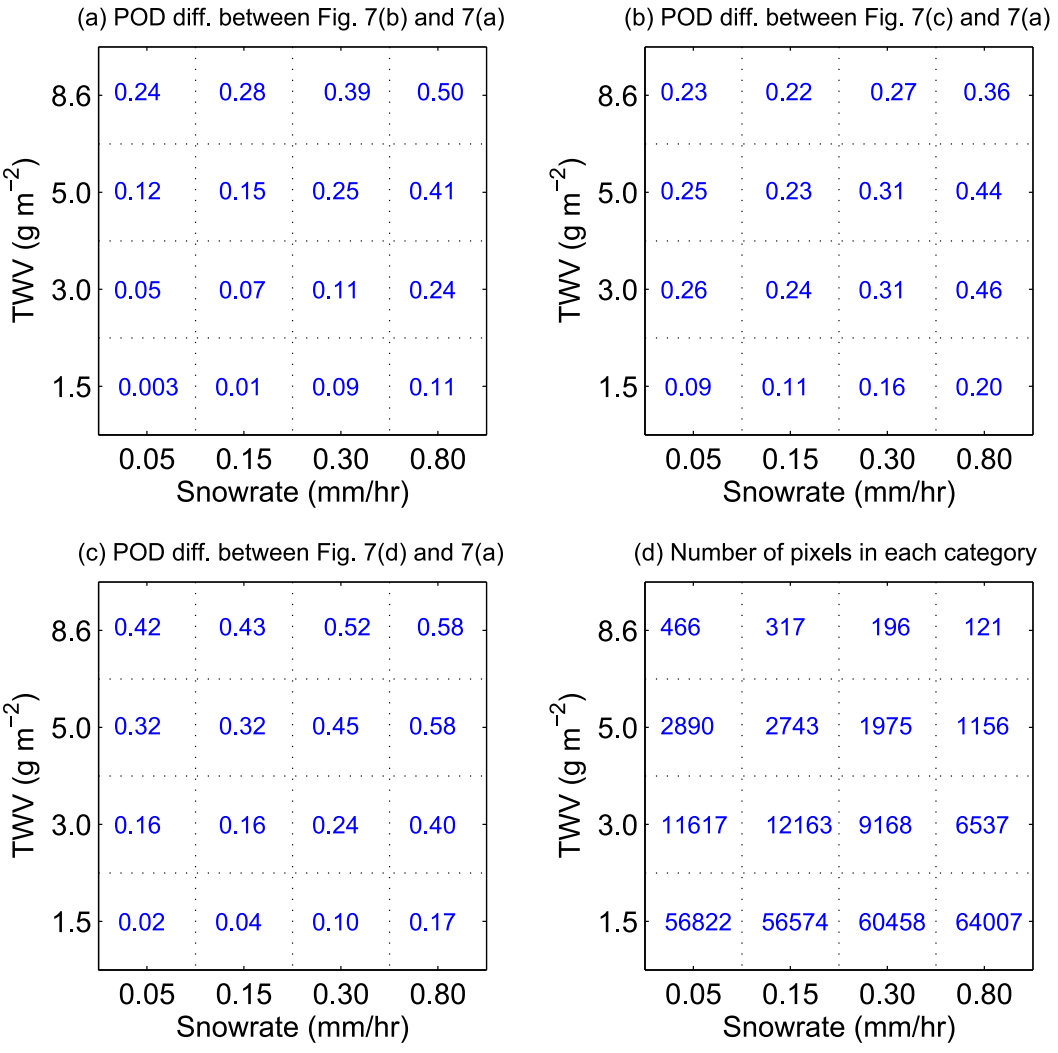

FIG. 8. Under different water vapor and snowfall intensity scenarios, (a) POD difference between the all-low-frequency-channel combination plus the V166 channel (Fig. 7b) and the all-low-frequency-channel combination (Fig. 7a), (b) POD difference between the all-low-frequency-channel combination plus the V183 ± 3 channel (Fig. 7c) and the all-low-frequency-channel combination (Fig. 7a), and (c) POD difference between the all-low-frequency-channel combination plus the V183 ± 7 channel (Fig. 7d) and the all-low-frequency-channel combination (Fig. 7a). (d) Number of pixels in each category.

improvement under these two scenarios (detailed explanation in the following section). In these two categories, the sample size (196 + 121 = 317 pixels) only accounts for about 0.1% of total sample. This explains why adding 89 GHz does not improve the POD when all of the data are used to perform the analysis (Fig. 6).

The aforementioned phenomenon (i.e., greater improvement by adding the V183 ± 3 channel to the low-frequency-channel set in relatively dry environments relative to adding the V166 and V183 ± 7 channels), suggests that the water vapor plays an important role in the snowfall detection process. We suggest that weak snowfall-scattering signatures are better captured by the V183 ± 3 channel because that channel is least sensitive to the surface (among the available channels on GMI) because of the water vapor mask effect. The next section describes a radiative transfer model simulation used to test this hypothesis.

3) RADIATIVE TRANSFER MODEL SIMULATION

A radiative transfer model (Liu 1998) has been used for several experiments to investigate the surface contamination, water vapor mask effect, and snowfall-scattering signals. This model calculates the TBs at different microwave frequencies through the discrete ordinate method at varying stream numbers. In the

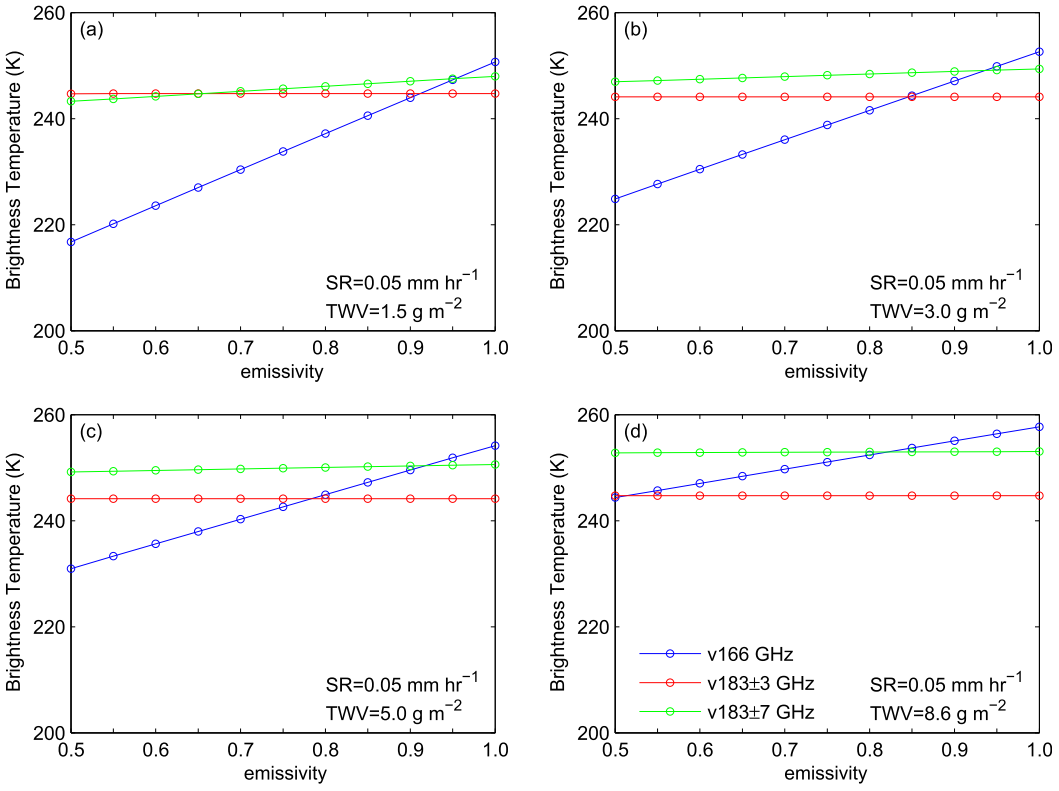

FIG. 9. Under different surface emissivities, simulated TBs at V166, V183 ± 3, and V183 ± 7, corresponding to 0.05 mm h^{-1} snowfall rate (SR) and TWV at (a) 1.5, (b) 3.0, (c) 5.0, and (d) 8.6 g m^{-2}. The correspondence between line color and TB channel is shown in (d).

current simulation, the stream number is set as 4. The water vapor absorptions from both line and continuum contributions are considered in this model. In addition, the sector-like shape (Liu 2008a) is used in the simulation. We have also tested six-bullet rosette and dendrite snowflake shape. The numerical values of the simulation change, but the main conclusions drawn from these simulations hold.

The TBs at V166, V183 ± 3, and V183 ± 7 are simulated, corresponding to the same surface snowfall rate (0.05, 0.15, 0.30, and 0.80 mm h^{-1}), but with surface emissivity increasing from 0.5 to 1.0 and TWV increasing from 1.5 to 8.6 g m^{-2}. This provides insight into the channel sensitivity to the water vapor mask effect, surface emissivity variation, and hydrometeor scattering effect. For the simulation, the surface temperature and temperature profile are obtained from MERRA data. The hydrometeor profile is from the KaPR observations. Above (below) the freezing level height, the hydrometeors are assumed to be in a solid (liquid) phase. No mixed phase hydrometeors are considered in the simulation. Figures 9 and 10 only show simulated results for snowfall rates at 0.05 and 0.8 mm h^{-1}. For snowfall rates at 0.15 and 0.30 mm h^{-1}, the simulated results are in between the results for snowfall rates at 0.05 and 0.80 mm h^{-1}.

Figure 9 shows that the surface emissivity variation strongly affects the TB at V166 when the environment is dry (TWV about 1.5 g m^{-2}) and the scattering signature is small (snowfall rate about 0.05 mm h^{-1}). Specifically, the TB at V166 increases by 34.0 K when surface emissivity increases from 0.5 to 1.0 (i.e., from 216.7 to 250.7 K; blue curve in Fig. 9a). With the same surface emissivity increase, the TB at V183 ± 7 also increases by ~4.7 K (green curve in Fig. 9a), whereas the V183 ± 3 TB remains almost constant (red curve in Fig. 9a). Thus, in dry winter environments with weak scattering signatures, adding the V183 ± 3 channel to the low-frequency-channel set increases the POD by 0.09 (bottom-left-corner value in Fig. 8b). Conversely, adding the V183 ± 7 and V166 channels only increases the POD by 0.02 (bottom-left-corner value in Fig. 8c) and 0.003 (bottom-left-corner value in Fig. 8a), respectively.

The surface influence on the V166 TB is largely reduced (assuming the same surface snowfall rates) in moist winter environments. Specifically, Fig. 9d shows

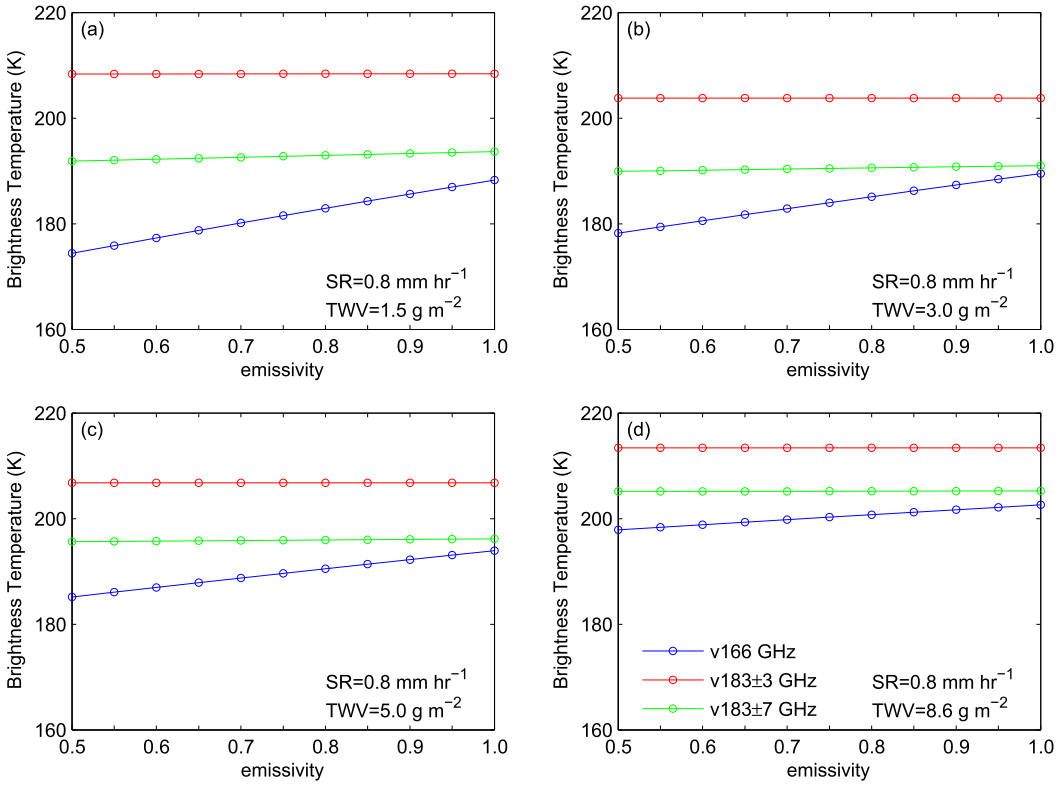

FIG. 10. As in Fig. 9, but for a 0.08 mm h^{-1} SR.

that the V166 TB only increases by 13.4 K (from 244.4 to 257.7 K; blue curve in Fig. 9d) in the moist winter environment, versus 34.0 K in the dry environment (blue curve Fig. 9a). Thus, the large amount of water vapor even makes the V166 channel less sensitive to the surface. In turn, this channel behaves like a low-level water vapor channel, as was noted by Bennartz and Bauer (2003) and Laviola and Levizzani (2011). In this scenario, the water vapor in the winter environment largely mitigates the surface influence for the V166 channel. Consequently, the POD increases by 0.24 (upper-left-corner value in Fig. 8a). This POD improvement is similar to adding the V183 ± 3 channel to the low-frequency-channel set (POD increases by 0.23; upper-left-corner value in Fig. 8b). Alternatively, in the moist winter environment, the surface emissivity variation has almost no influence on the TB at 183 ± 7 GHz (green curve in Fig. 9d). The scattering signature is also smaller at V183 ± 3 than at V183 ± 7 because of the water vapor mask effect (discussed next). Therefore, adding the V183 ± 7 channel provides much more improvement to the POD (0.42; upper-left-corner value in Fig. 8c) than adding the V183 ± 3 channel (0.23; upper-left-corner value in Fig. 8b). While the water vapor can mask or alleviate the surface contamination, it also reduces the scattering signature. For example, for a TWV of 1.5 g m^{-2} and a surface emissivity of 0.5, the 183 ± 7 GHz TB decreases by about 51.4 K from 243.3 to 191.9 K (cf. Fig. 9a and Fig. 10a), along with the snowfall rate increasing from 0.05 to 0.8 mm h^{-1}. In contrast, at the 183 ± 3 GHz TB decreases by 36.3 K from 244.7 to 208.4 K. Bennartz and Bauer (2003) reported a similar finding.

When the winter environment is moist (TWV about 8.6 g m^{-2}) and the scattering signature is large (i.e., snowfall rate of about 0.8 mm h^{-1}), even the V166 TB does not vary much with the surface emissivity variation. In fact, the TB at V166 only increases by about 4.7 K from 197.9 to 202.6 K when surface emissivity increases from 0.5 to 1.0 (blue curve in Fig. 10d). In this case, adding the V166 channel to the low-frequency-channel set increases the POD by 0.50 (upper-right-corner value in Fig. 8a), versus an increase of only 0.36 that results from adding the V183 ± 3 channel (upper-right-corner value in Fig. 8b).

In short, there are two competing factors for snowfall detection over land. Surface contamination is the first, and the second is the scattering signatures from the suspended ice particles. Because of the relatively weak scattering signature from snowfall (compared with that from rainfall), the surface contamination can significantly affect the snowfall detection performance from

TABLE 3. POD derived from water vapor band channels (V183 ± 3 and V183 ± 7), high-frequency window channels (V89, H89, V166, and H166), and high-frequency channels (i.e., water vapor band channels plus high-frequency window channels).

Channel availability	POD
High-frequency water vapor channels	0.13
High-frequency window channels	0.66
High-frequency channels (water vapor + window)	0.74

the passive microwave radiometers. Fortunately, the water vapor can effectively mask out, or at least alleviate, the surface contamination for the water vapor band channels (V183 ± 3 and V183 ± 7), depending on the amount of water vapor in the air. This water vapor mask effect largely accounts for the greater snowfall detection improvement by adding the V183 ± 3 channel to the low-frequency-channel set.

In the model simulation, we did not consider the effect of supercooled liquid water. As mentioned in the introduction, previous work (Kulie et al. 2010; Löhnert et al. 2011; Xie et al. 2012; Liu and Seo 2013; Wang et al. 2013) has shown that the liquid water can further complicate the snowfall detection by increasing the TB at the high-frequency channels. Therefore, the columnar cloud liquid water could reduce or mute the scattering effects observed in the modeling exercise if the liquid water is taken into consideration.

4) SNOWFALL DETECTION PERFORMANCE FROM THE WATER VAPOR CHANNELS

Of all the high-frequency channels, the POD improves the most by adding the V183 ± 3 channel to the low-frequency-channel set. However, using the water vapor channels (V183 ± 3 and V183 ± 7) alone does not provide the best snowfall detection. Table 3 shows the PODs derived from only the water vapor channels (V183 ± 3 and V183 ± 7), from the high-frequency window channels (V89, H89, V166, and H166), and from all high-frequency channels (both water vapor and window channels). As expected, the POD is very small (0.13) when using only the water vapor channels. Alternatively, the POD is 0.66 when using only the high-frequency window channels. Combining these two sets of channels improves the POD to 0.74. This suggests that the scattering signature from the high-frequency window channels is essential for snowfall detection and that the water vapor mask effect is required to achieve optimal snowfall detection performance.

To further demonstrate the snowfall detection capability of the water vapor channels alone, Fig. 11 shows the snowfall detection performance for the three snowfall cases discussed in section 4a. The water vapor channels almost completely missed the snowfall event over the Great Lakes region, as indicated by the ground observations (magenta crosses in Fig. 11a), KuPR (green dots in Fig. 11b), and KaPR (red dots in Fig. 11c). These channels alone also falsely identified snowfall between 35° and 40°N, where ground stations, KuPR, and KaPR reported no snowfall. For the snow event in China, the water vapor channels missed most of the snowfall pixels indicated by the other sensors and falsely identified snowfall pixels around Beijing. For the snowfall case over Siberia, Russia, the water vapor channels captured most of the snowfall pixels, but falsely identified snowfall pixels south of 50°N.

The snowfall occurrence frequency is also calculated for each 1° grid box using only the water vapor channels (Fig. 17d, described in greater detail below) and the KaPR observations (Fig. 17a, described in greater detail below). Using only the water vapor band channels misses many snowfall events over North America and East Asia and falsely identifies snowfall over Siberia, Russia (e.g., near 60°N, 120°E). It is worth mentioning that the geospatial distribution of the snowfall occurrence frequency from the water vapor channels alone is shown in Fig. 17 (described in greater detail below), instead of in the immediately following figure, because we would like to demonstrate snowfall detection performance difference from six types of radiometers in the GPM constellation.

In summary, when TWV is relatively small, the greatest snowfall detection improvement results from adding the V183 ± 3 channel to the low-frequency-channel set (V10, H10, V19, H19, V24, V37, and H37) (vs adding the V166 and V183 ± 7 channels). For environments with more water vapor, the greatest snowfall detection improvement results from adding the V183 ± 7 channel. In very moist winter environments (TWV around 8.6 g m^{-2}) adding the V166 channel improves the snowfall detection performance even more than by adding the V183 ± 3 channel. This observation is explained by the competing effects of surface contamination and the snowfall-scattering signature. In relatively dry environments, there is only enough water vapor to mask the surface effect for the V183 ± 3 channel. More water vapor can effectively mask the influence of the surface for the V183 ± 7 channels. In very moist winter environments, the large amount of water vapor makes the V166 channel almost blind to the surface, so this channel better captures the scattering signature from snowfall. The radiative transfer model simulation supports this explanation.

Both case studies and the snowfall occurrence frequency geospatial distribution demonstrated that the water vapor channels alone contain very little snowfall detection information. In contrast, the high-frequency

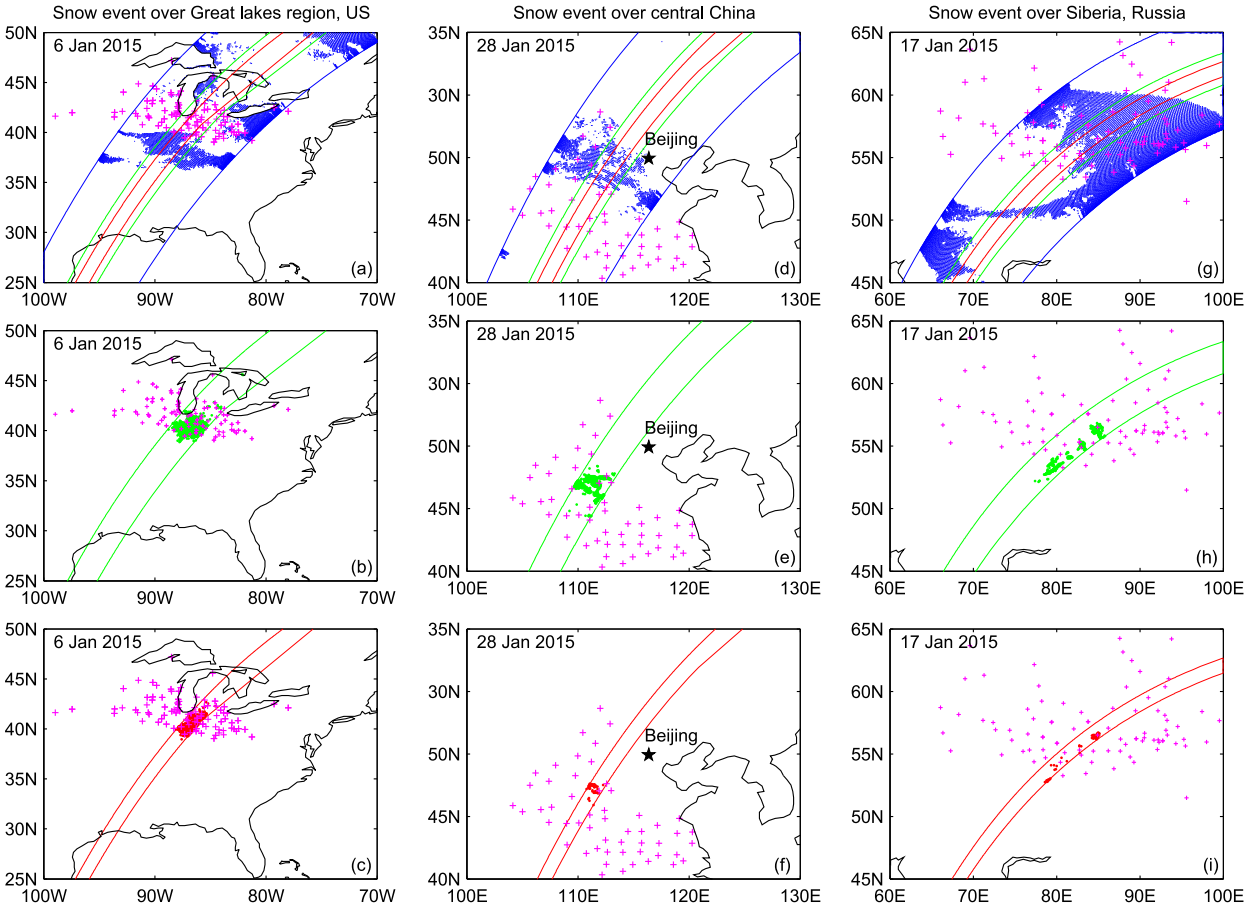

FIG. 11. As in Fig. 4, but for snowfall occurrence frequency in (a), (d), and (h) derived from water vapor channels (type-6 radiometer).

window channels (89 and 166 GHz) have much larger snowfall detection capability, which implies that the scattering signal, not the water vapor mask effect, is essential for snowfall detection. Combining the 183-GHz water vapor channels with the high-frequency window channels (89 and 166 GHz) captures the snowfall-scattering signal while accounting for the water vapor mask effect.

5. Snowfall detection performance from all possible channel combinations

We next examine the PODs for all possible channel combinations. There are 8191 possible channel combinations from the 13 GMI channels ($C_{13}^1 + C_{13}^2 + \ldots + C_{13}^{13} = 8191$). These combinations are labeled as "channel combination index" in Fig. 12. PODs from several typical channel combinations are also labeled in Fig. 12a. The PODs vary greatly from 0.02 to 0.77. The PODs less than 0.35 are mostly from the low-frequency-channel combinations (V10, H10, V19, H19, V24, V37, H37, V89, and H89) or water vapor channels. No single channels have PODs greater than 0.22, regardless of the frequency.

Channel availability is analyzed for channel combinations with POD greater than 0.70 (horizontal red dashed line in Fig. 12a). There are 805 channel combinations with POD greater than 0.70, and Fig. 12b illustrates their channel availability. As expected, the V166 and H166 channels appear in all 805 channel combinations. The V89 and H89 channels are the second most common (~75%). This again shows that the scattering signature in the 166 and 89 channels is indispensable for snowfall detection. Without these four channels, the largest possible POD is 0.52. This result is consistent with a sensitivity study by Mejia et al. (2008). They showed that the snowfall detection performance of AMSU-B is noticeably worse without 89 GHz and 150 channels.

6. Snow detection capability of the GPM constellation radiometers

a. GPM constellation radiometers

At the launch of the GPM core satellite, the GPM radiometer constellation includes 13 passive microwave

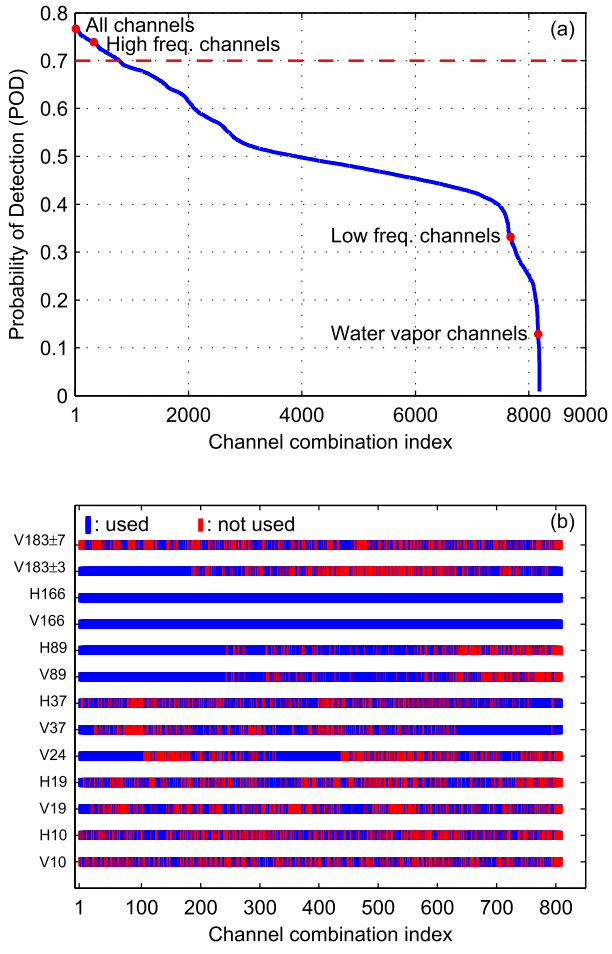

FIG. 12. (a) Ranked POD values from 8191 (all possible) GMI channel combinations. (b) Channel availability in each of the 805 combinations with POD larger than 0.70.

radiometers (Hou et al. 2014; Kummerow et al. 2015). Table 1 provides attributes for the WindSat, Advance Microwave Sounding Unit-A (AMSU-A), Advanced Microwave Scanning Radiometer for Earth Observing System (AMSR-E), Advanced Microwave Scanning Radiometer-2 (AMSR2), TRMM Microwave Imager (TMI), Special Sensor Microwave Imager (SSM/I), AMSU-B, MHS, Microwave Analysis and Detection of Rain and Atmospheric Systems (MADRAS), SSMIS, GMI, ATMS and Sondeur Atmosphérique du Profil d'Humidité Intertropicale par Radiométrie (SAPHIR).

These 13 radiometers can be grouped into six categories based on the channel availability: 1) low-frequency channels only (WindSat); 2) low-frequency channels plus the 89-GHz channel (TMI, AMSR-E, AMSR2, AMSU-A, and SSMI); 3) high-frequency channels only (AMSU-B and MHS); 4) all channels (SSMIS, GMI, and ATMS); 5) all channels except 183-GHz channels (MADRAS); and 6) 183 GHz water vapor band channels (SAPHIR). Although MADRAS and SAPHIR only cover the tropics, where snowfall occurrence only exists over some mountainous regions, these two types of radiometers are retained as comparison references for the other sensors. For convenience, these six types of radiometers are referred to as type-1 radiometer (low-frequency channels), type-2 radiometer (low-frequency channels + 89 GHz), type-3 radiometer (high-frequency channels), type-4 radiometer (all channels), type-5 radiometer (all channels except 183-GHz channels), and type-6 radiometer (183-GHz channels).

Several aspects differ among these radiometers. For example, the footprint size varies greatly despite their similar frequencies. Also, some sensors employ a conical scanning scheme (e.g., SSMIS, TMI, and GMI), while others use a cross-track scanning scheme (e.g., ATMS, MHS, and SAPHIR). Ideally, one would collocate these 13 radiometers to a common snowfall observation reference to judge their snowfall detection capability. For example, over the continental United States, the ground radar observations can serve as the common reference. However, there is no such a reference on the global scale. Therefore, in this study, subsets of GMI channels are used to estimate the snowfall detection capability for these six types of radiometers with common frequencies. The authors would like to emphasize that the essential idea here is not to obtain the exact POD value of each radiometer. Instead, the idea is to rank these six types of radiometers, which serve as ''prototype'' sensor types for future sensors that could be added to the constellation.

The GMI frequencies range from 10 to 183 ± 7 GHz, which are commonly available from the other 12 radiometers. Table 1 lists the frequency and polarization for each radiometer. The channels around 6.9 and 50.3 GHz are unavailable from GMI. Since the low-frequency channels contain very limited snowfall detection information (because of the surface contamination, reduced sensitivity to the scattering signature, and the larger FOV at low-frequency channels), omitting these channels likely does not significantly affect the statistics shown below.

At similar frequencies, for almost all channels the GMI has the finest pixel resolution of the 13 radiometers. Occasionally, the FOV on a certain radiometer at a specific frequency is slightly finer than that from GMI. For example, the FOV at the V37 channel on WindSat is 10 versus 12 km on GMI (Gaiser et al. 2004; Draper et al. 2015). In addition, the other 12 radiometers also are calibrated against the GMI (Biswas et al. 2013). Thus, it is likely that the snow detection skills for the other 12 radiometers estimated by subsets of

TABLE 4. POD values for the six types of GPM constellation radiometer (Table 1).

Radiometer type	POD	Typical radiometer	Channel availability
1	0.33	WindSat	Low-frequency channels
2	0.43	TMI	Low-frequency channels + 89 GHz
3	0.74	MHS	High-frequency channels
4	0.77	GMI	All channels
5	0.72	MADRAS	All channels except 183-GHz channels
6	0.13	SAPHIR	183-GHz channels

GMI channels represent their upper-bound detection capability.

b. *PODs of the GPM constellation radiometers*

Table 4 lists the POD values from the six types of radiometers. The type-6 radiometer (183-GHz water vapor channels) has the poorest snowfall detection performance (POD at 0.13). This finding again suggests that the high-frequency window channels (89 and 166 GHz) are necessary to effectively capture the scattering signature and improve snowfall detection. The POD is 0.33 for the type-1 radiometer (low-frequency channels). For the type-2 radiometer (low-frequency channels + 89 GHz), the POD improves to 0.42. However, adding either V89 or H89 alone does not improve the POD (Fig. 6). The addition of both channels to the low-frequency-channel set is what increases the POD to 0.42. Previous studies have also noted the relatively poor detection performance from the V10–V89 channels (Liu and Curry 1997; Skofronick-Jackson et al. 2013).

Both the type-5 radiometer (all channels except 183 channels) and type-3 radiometer (high-frequency channels) possess much better snowfall detection capability than the type-1 radiometer (low-frequency channel only) and type-2 radiometer (low-frequency channels + 89 GHz), with PODs of 0.72 and 0.74, respectively. The snowfall detection improvement demonstrates the much stronger response from the high-frequency channels.

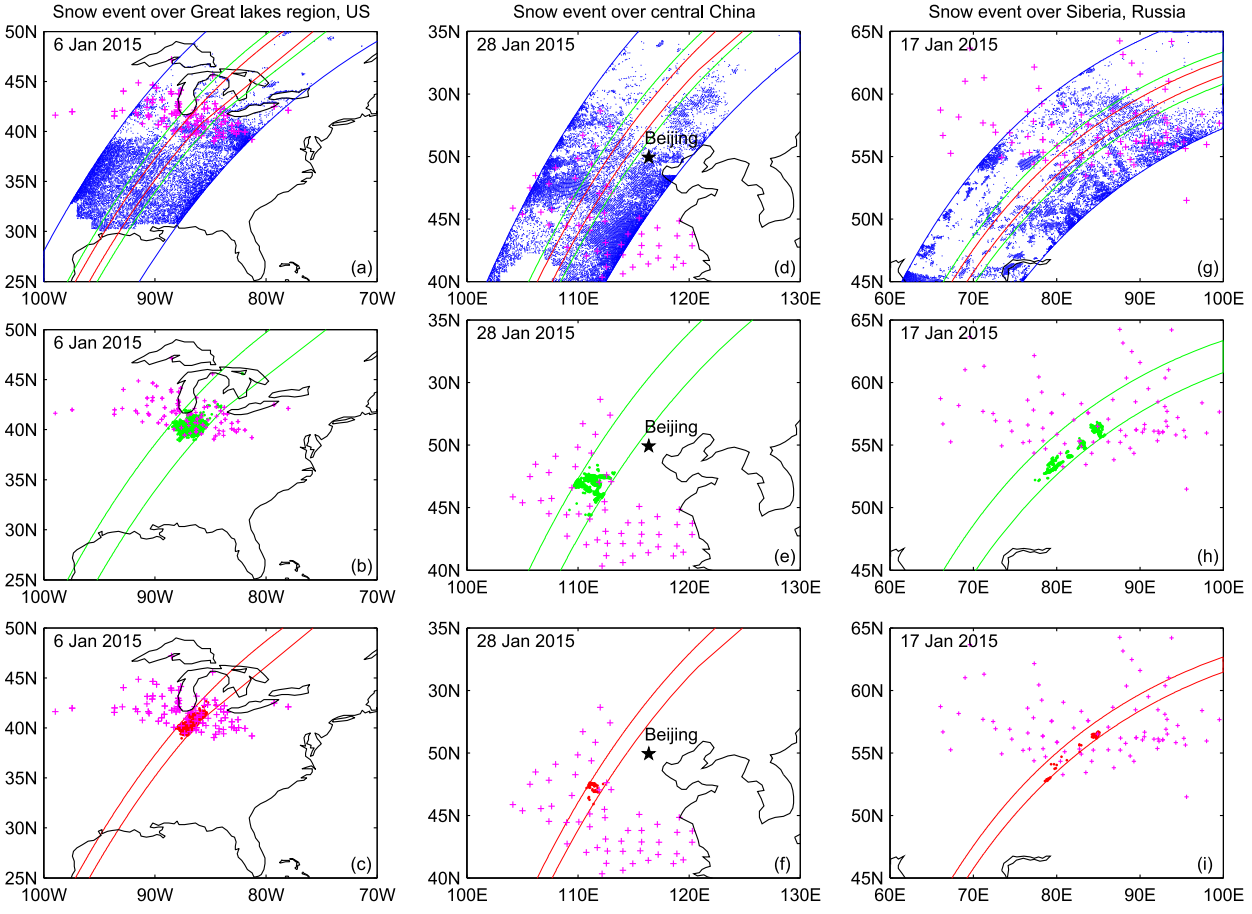

FIG. 13. As in Fig. 4, but for snowfall occurrence in (a), (d), and (h) derived from the type-2 radiometer (low-frequency channels + 89 GHz).

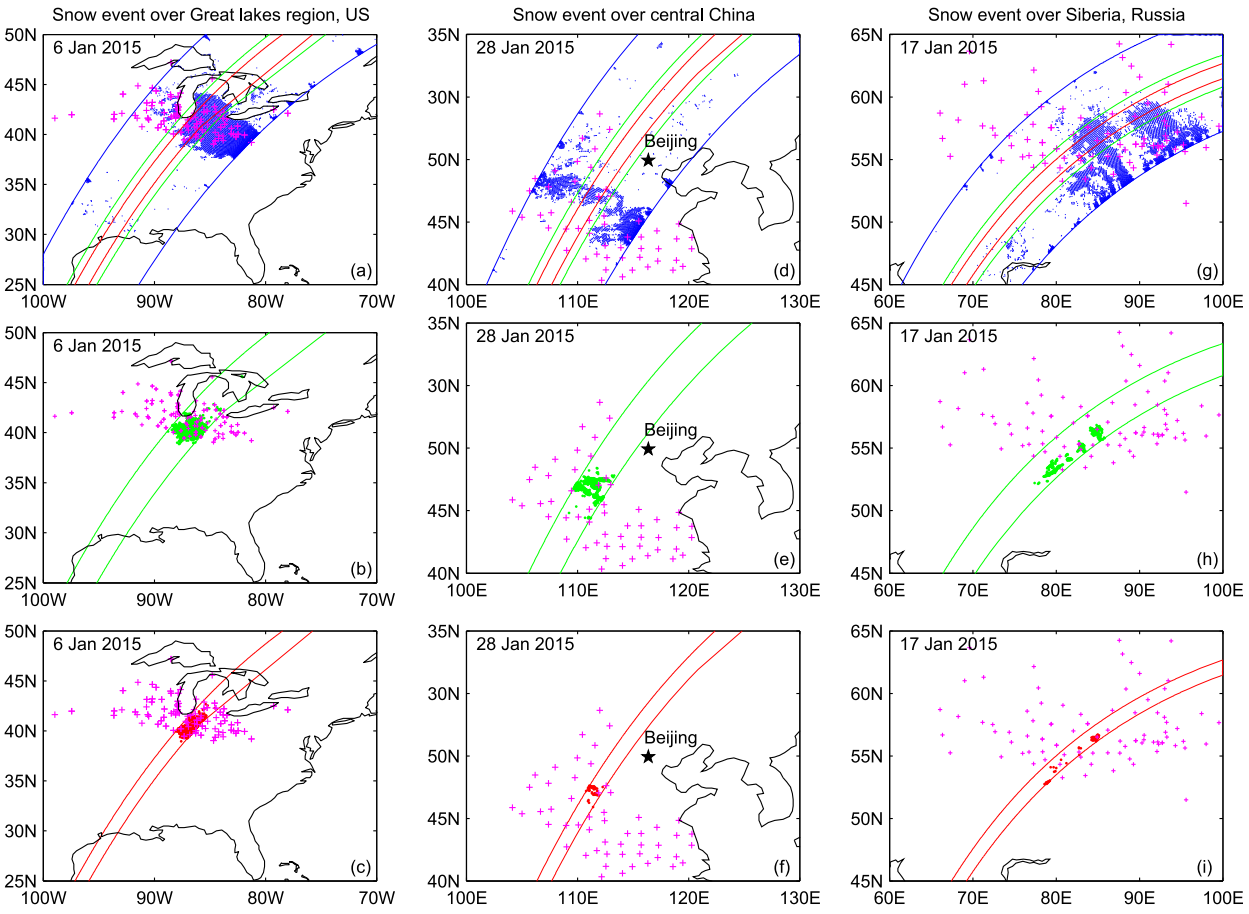

FIG. 14. As in Fig. 4, but for snowfall occurrence in (a), (d), and (h) derived from the type-4 radiometer (all channels).

For the type-5 radiometer (all channels except 183 channels), the scattering signature from the high-frequency channels contributes much of the snowfall detection skill. As shown previously, for the type-3 radiometer (high-frequency channels), both the scattering effect (mainly from the window channels; e.g., V166) and water vapor mask effect (183 vapor bands) contribute to the better snowfall detection. The type-4 radiometer (all channels; e.g., GMI, ATMS, and SSMIS) provide the best snowfall detection (POD of 0.77).

Additionally, the POD from the type-3 radiometer (high-frequency channels) is only slightly larger than that from the type-4 radiometer (all channels), which indicates that the low-frequency channels are of less importance. Further, the POD from the type-4 radiometer (all channels) is only 0.05 larger than that from the type-5 radiometer (all channels except 183 channels). This supports our earlier finding that the scattering signature from the high-frequency window channels is more important for snowfall detection than the water vapor signature from the 183-GHz channels.

c. *Case studies and geospatial distribution of the snowfall occurrence frequency*

We next revisit the three snowfall cases in the Great Lakes; eastern China; and Siberia, Russia, to demonstrate the snowfall detection performances by these six types of radiometers (Figs. 4, 11, 13–16). The type-1 radiometer (low-frequency channels; Fig. 4), type-6 radiometer (183-GHz channels; Fig. 11), and type-2 radiometer (low-frequency channels + 89 GHz; Fig. 13) perform poorest for these cases. The greatest limitation of these sensors is the large number of false snowfall detections. Alternatively, the type-4 radiometers (all channels; Fig. 14), the radiometer, KuPR, KaPR, and ground observations agree very well during these cases. For example, the radiometer clearly captures the snowfall event over the Great Lakes on 6 January 2015 (blue dots in Fig. 14a), which was also observed by the ground stations (magenta cross in Figs. 14a–c), KuPR (green dots in Fig. 14b), and KaPR (red dots in Fig. 14c). More importantly, it almost completely eliminates the false identification of the snowfall that was evident in

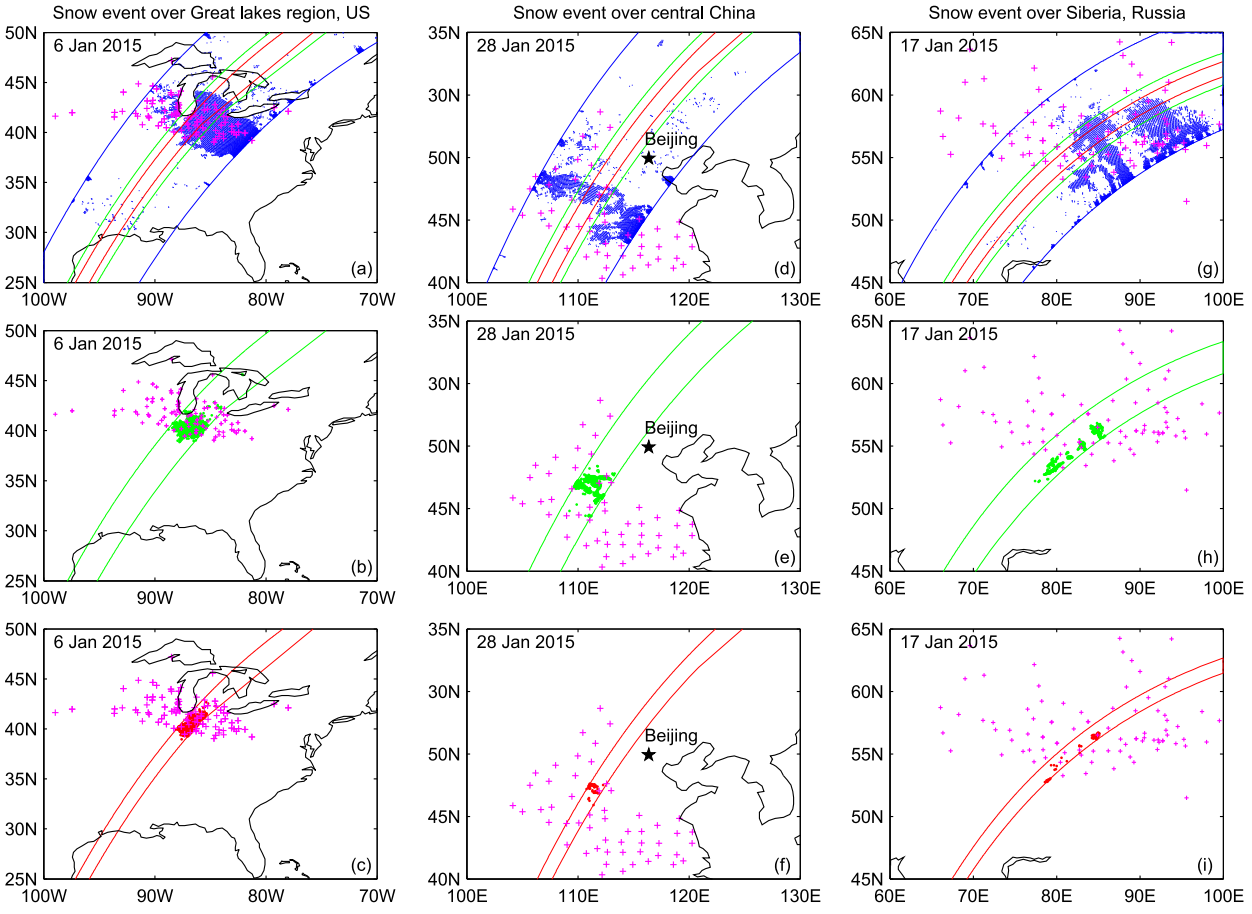

FIG. 15. As in Fig. 4, but for snowfall occurrence in (a), (d), and (h) derived from the type-3 radiometer (high-frequency channels).

Figs. 4a, 4d, and 4g and Figs. 11a, 11d, and 11g. For the type-3 radiometer (all high-frequency channels; Fig. 15) and type-5 (all channels except 183-GHz channels; Fig. 16), the snowfall detection skills are very similar to those from the type-4 radiometers (all channels). An exception is that the type-5 radiometer (all channels except 183-GHz channels; Fig. 16) contains more falsely identified snowfall pixels in the lower portion of the swath in the Great Lakes (cf. Fig. 14a and Fig. 16a). These falsely identified snowfall pixels are very likely caused by the surface contamination. This further demonstrates that the high-frequency water vapor channels (183 GHz) are necessary to achieve the optimal snowfall detection.

Spatial snowfall occurrence frequencies are calculated for the six types of radiometers (Figs. 5 and 17). The occurrence frequency derived from the type-4 radiometer (all channels; Fig. 17b) agrees best with that from the KaPR observations (Fig. 17a). Similar patterns from the type-3 and type-5 radiometers are noticed (not shown). However, the spatial occurrence frequency from the type-1 radiometers (low-frequency channels; Fig. 5b) and the type-2 radiometers (low-frequency channels + 89 GHz; Fig. 17c) are the opposite of the KaPR observations. Specifically, the snowfall occurrence frequencies from these two types of sensors are smaller in the high-latitude regions (north of 45°N), and larger in the low-latitude regions. For example, both the type-1 and type-2 radiometers greatly underestimate the snowfall occurrence frequency in Alaska, northeastern Canada, the western portion of Russia, and the Kamchatka Peninsula, while snowfall frequency overestimates are evident from the Black Sea to the Caspian Sea. As noted previously, using only the 183-GHz water vapor band channels (Fig. 17d) misses many snowfall pixels in North America and falsely identifies snowfall in Siberia, Russia.

To summarize, it is found that the type-4 radiometers (all channels; SSMIS, GMI, and ATMS) possess the best snowfall detection capability, followed by type-3 radiometers (high-frequency channels) and type-5 radiometers (all channels except 183-GHz channels). The type-1 radiometer (low-frequency channels), type-2 radiometer

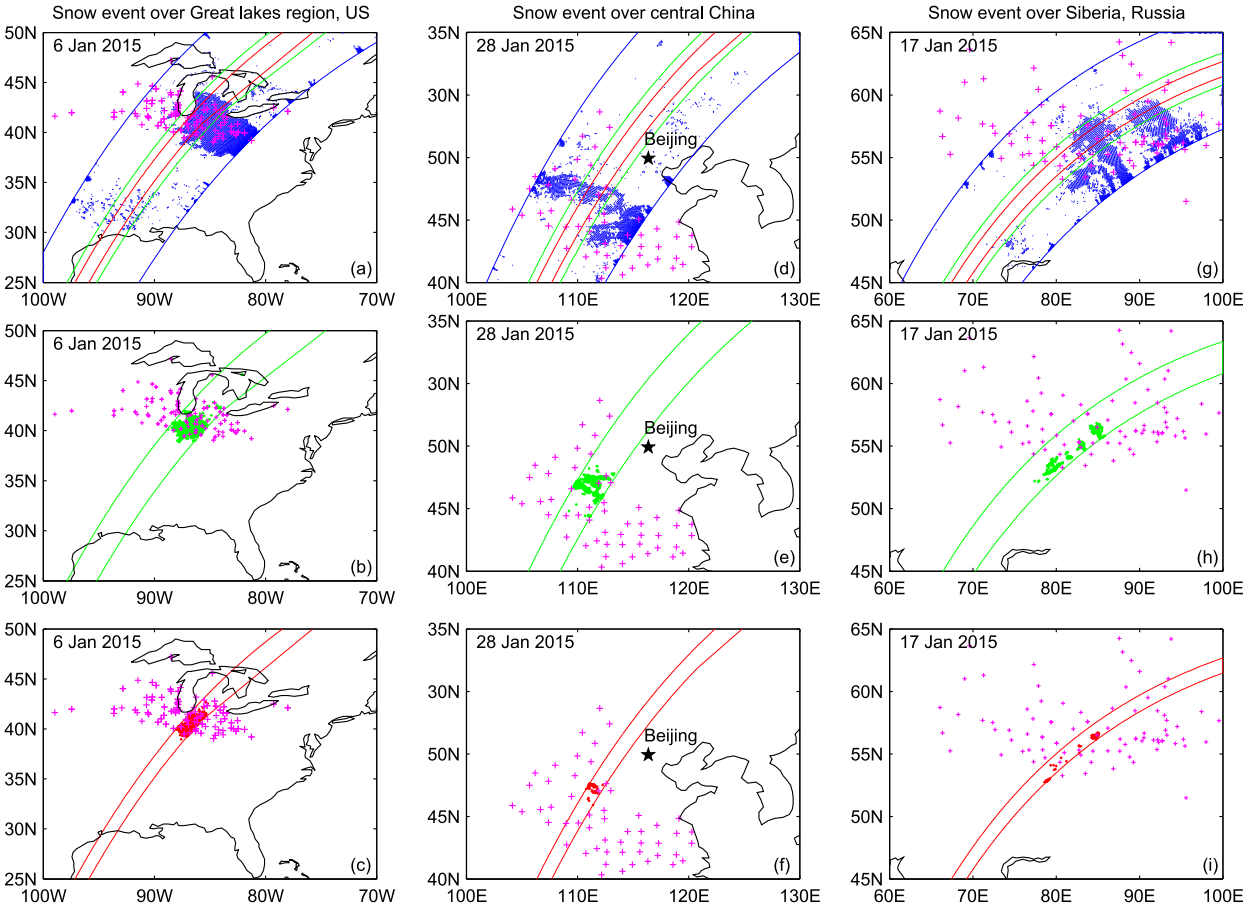

FIG. 16. As in Fig. 4, but for snowfall occurrence in (a), (d), and (h) derived from the type-5 radiometer (all channels except 183 channels).

(low-frequency channels + 89 GHz), and type-6 radiometer (183-GHz channels only) performed the poorest.

7. Conclusions and discussion

This study quantified the microwave channels' snowfall detection capability from an observational perspective by using data from GPM's DPR and GMI. To judge the snowfall detection performance for different channels or channel combinations, the POD is taken as the metric, corresponding to the same FAR at 0.1.

We first evaluated the snowfall detection skill from the low-frequency channel or channel combinations. Results showed that the low-frequency channels (V10, H10, V19, H19, V24, V37, and H37) contain limited snowfall detection information (POD at 0.34), which frequently miss the snowfall occurrence while falsely identifying snowfall, compared with observations from ground station, KuPR, and KaPR.

To demonstrate the importance of the high-frequency channels, the high-frequency channels (V89, H89, V166, H166, V183 ± 3, and V183 ± 7) are added to the low-frequency-channel set (V10, H10, V19, H19, V24, V37, and H37) one by one. It was found that adding the V183 ± 3 channel provided the greatest improvement, by which POD increases from 0.34 to 0.50. This result differs from previous theoretical studies, which showed that the strongest scattering signature is from the high-frequency window channel (e.g., V166). We suggested that the weak snowfall-scattering signal is better captured by the V183 ± 3 channel, because the V183 ± 3 channel is the least sensitive channel (among the available channels on GMI) to the surface due to the water vapor mask effect. The statistical analysis under different water vapor and snowfall intensity scenarios and the radiative transfer model simulations support this explanation.

Adding the V183 ± 3 channel to the low-frequency-channel set provides the larger POD improvements, compared with adding V166 and V183 ± 7 channels. However, this does not imply that the water vapor effect is the key element for snowfall detection. In fact,

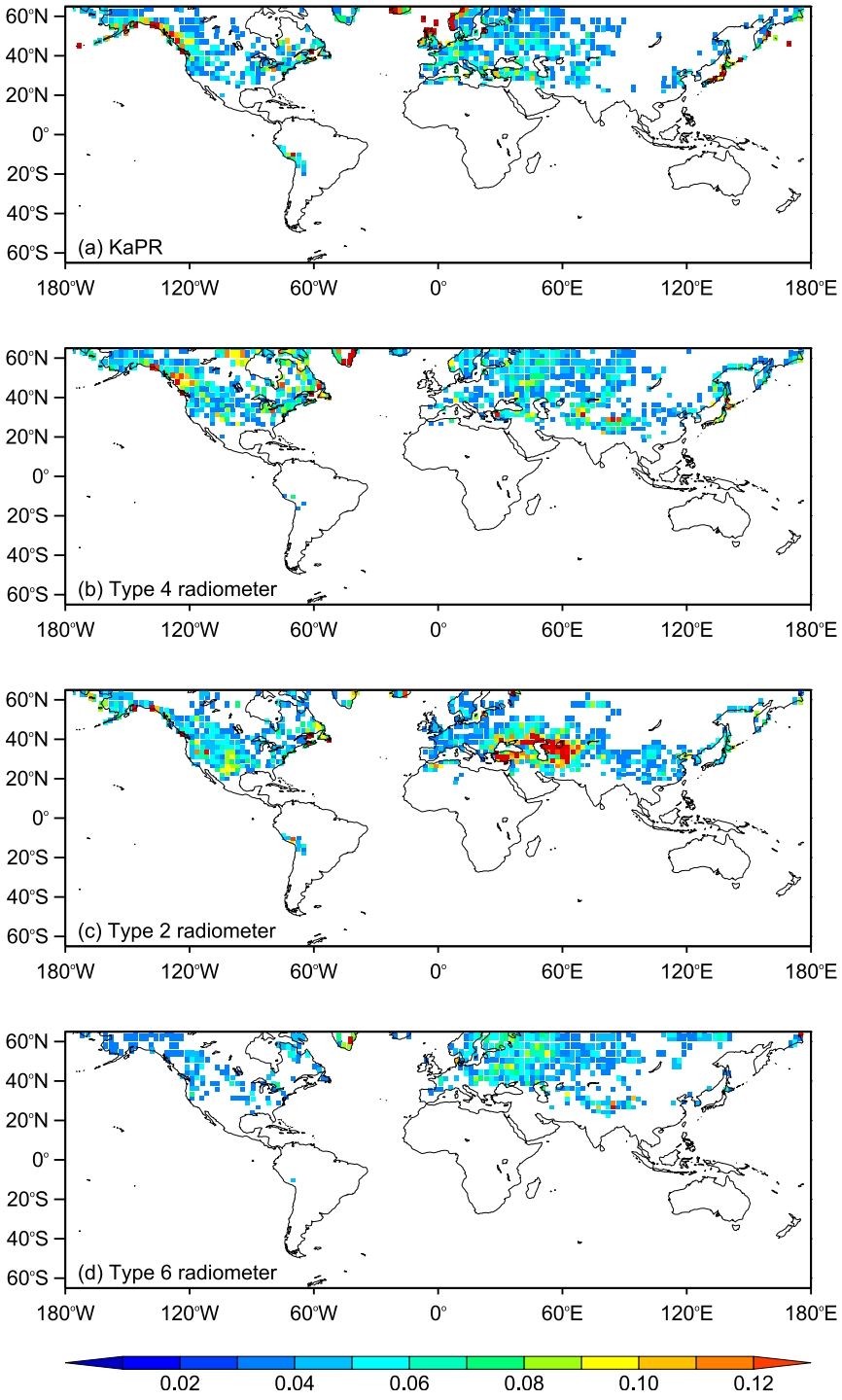

FIG. 17. (a) Geospatial distribution of snowfall occurrence frequency derived from KaPR. (b) Geospatial distribution of snowfall occurrence frequency derived from the type-4 radiometer (all channels). The patterns derived from the type-3 radiometers (high-frequency channels) and type-5 radiometers (all channels except 183-GHz channels) are almost identical to those from the type-4 radiometers (all channels). (c) As in (b), but for the type-2 radiometer (low-frequency channels + 89 GHz). (d) As in (b), but for the type-6 radiometer (183-GHz channels). See Table 1 for more details regarding the definition of the radiometer type.

only employing the 183 GHz water vapor band channels (V183 ± 3 and V183 ± 7), the snowfall detection skill is very low with POD at 0.13. On the other hand, using the high-frequency window channels (V89, H89, V166, and H166), the POD is 0.66. These results suggest that water vapor masks/alleviates the surface contamination, while scattering signature is essential for snowfall detection.

The PODs from all 8191 possible channel combinations are calculated. It is noticed that V166 and H166 appear in any channel combination with a POD greater than 0.7. Channels V89 and H89 appear in the majority of these combinations. These results further demonstrate that the scattering signature is the key element for snowfall detection.

The GPM constellation radiometers are grouped into six types (Table 1), based on the channel availability. Subsets of GMI channels are used to estimate the snowfall detection capability of each type. The type-4 radiometer (all channels) performs the best for snowfall detection, followed by the type-3 radiometer (high-frequency channels) and the type-5 radiometer (all channels except 183-GHz channels). The type-1 radiometer (low-frequency channels), type-2 radiometer (low-frequency channels + 89 GHz), and type-6 radiometer (183-GHz channels only) show limited snowfall detection capability.

The improved snowfall detection performance from the type-4 radiometer (all channels) is further demonstrated by snowfall case studies and the snowfall occurrence frequency geospatial distribution. The snowfall identification from the type-4 radiometer agrees well with that from ground station, KuPR, and KaPR observations. More importantly, the prevalent false identification by the type-1, type-2, and type-6 radiometers is almost completely eliminated. The type-3 (high-frequency channels) and type-5 (all channels except 183-GHz channels) radiometers perform similarly to the type-4 radiometers (all channels).

In this study, the KaPR snowfall detection is taken as the reference (truth). With a minimum detection of ~12 dBZ, KaPR will miss most of the light snowfall. Studies have shown that *CloudSat* is the most reliable space-based snowfall detection instrument currently available (Liu 2008b; Kulie et al. 2016), with a minimum detection reflectivity at ~−28 dBZ. However, the collocated sample size between GMI and *CloudSat* is limited. Future work will seek to extend this work over both land and ocean by combining KaPR and *CloudSat* snowfall observations.

This work can be easily adapted to evaluate the GMIs snowfall detection capability over the ocean in the future. In addition, this study indicates that for the upcoming microwave sensor design, the high-frequency window channels (e.g., 166 GHz) are indispensable for snowfall detection over land. The 183 GHz water vapor channels are necessary to obtain the optimal snowfall detection performance, and the low-frequency channels are of less importance.

Acknowledgments. GPM data were downloaded from NASA Precipitation Processing System (PPS) website (https://storm.pps.eosdis.nasa.gov/storm/). This study was supported by NOAA Grant NA14NES4320003 [Cooperative Institute for Climate and Satellites (CICS)] at the University of Maryland/ESSIC. The contents of this paper are solely the opinions of the authors and do not constitute a statement of policy, decision, or position on behalf of NOAA or the U.S. government. We thank the constructive and valuable comments from the anonymous reviewers.

REFERENCES

Adler, R. F., G. J. Huffman, and P. R. Keehn, 1994: Global tropical rain estimates from microwave-adjusted geosynchronous IR data. *Remote Sens. Rev.*, **11**, 125–152, doi:10.1080/02757259409532262.

Behrangi, A., Y. Tian, B. H. Lambrigtsen, and G. L. Stephens, 2014: What does *CloudSat* reveal about global land precipitation detection by other spaceborne sensors? *Water Resour. Res.*, **50**, 4893–4905, doi:10.1002/2013WR014566.

Bennartz, R., and P. Bauer, 2003: Sensitivity of microwave radiances at 85–183 GHz to precipitating ice particles. *Radio Sci.*, **38**, 8075, doi:10.1029/2002RS002626.

Biswas, S. K., S. Farrar, K. Gopalan, A. Santos-Garcia, W. L. Jones, and S. Bilanow, 2013: Intercalibration of microwave radiometer brightness temperatures for the Global Precipitation Measurement mission. *IEEE Trans. Geosci. Remote Sens.*, **51**, 1465–1477, doi:10.1109/TGRS.2012.2217148.

Chen, F. W., and D. H. Staelin, 2003: AIRS/AMSU/HSB precipitation estimates. *IEEE Trans. Geosci. Remote Sens.*, **41**, 410–417, doi:10.1109/TGRS.2002.808322.

Di Michele, S., and P. Bauer, 2006: Passive microwave radiometer channel selection based on cloud and precipitation information content. *Quart. J. Roy. Meteor. Soc.*, **132**, 1299–1323, doi:10.1256/qj.05.164.

Draper, D. W., D. Newell, F. J. Wentz, S. Krimchansky, and G. M. Skofronick-Jackson, 2015: The Global Precipitation Measurement (GPM) Microwave Imager (GMI): Instrument overview and early on-orbit performance. *IEEE J. Sel. Top. Appl. Earth Obs. Remote Sens.*, **8**, 3452–3462, doi:10.1109/JSTARS.2015.2403303.

Ferraro, R. R., N. C. Grody, and G. F. Marks, 1994: Effects of surface conditions on rain identification using the DMSP-SSM/I. *Remote Sens. Rev.*, **11**, 195–209, doi:10.1080/02757259409532265.

Foster, J. L., and Coauthors, 2012: Passive microwave remote sensing of the historic February 2010 snowstorms in the middle Atlantic region of the USA. *Hydrol. Processes*, **26**, 3459–3471, doi:10.1002/hyp.8418.

Fu, Y., and G. Liu, 2001: The variability of tropical precipitation profiles and its impact on microwave brightness temperatures as inferred from TRMM data. *J. Appl. Meteor.*, **40**, 2130–2143, doi:10.1175/1520-0450(2001)040<2130:TVOTPP>2.0.CO;2.

Gaiser, P. W., and Coauthors, 2004: The WindSat spaceborne polarimetric microwave radiometer: Sensor description and

early orbit performance. *IEEE Trans. Geosci. Remote Sens.*, **42**, 2347–2361, doi:10.1109/TGRS.2004.836867.

Grody, N. C., 1991: Classification of snow cover and precipitation using the Special Sensor Microwave Imager. *J. Geophys. Res.*, **96**, 7423–7435, doi:10.1029/91JD00045.

Hamada, A., and Y. N. Takayabu, 2016: Improvements in detection of light precipitation with the Global Precipitation Measurement Dual-Frequency Precipitation Radar (GPM DPR). *J. Atmos. Oceanic Technol.*, **33**, 653–667, doi:10.1175/JTECH-D-15-0097.1.

Hou, A. Y., and Coauthors, 2014: The Global Precipitation Measurement mission. *Bull. Amer. Meteor. Soc.*, **95**, 701–722, doi:10.1175/BAMS-D-13-00164.1.

Kacimi, S., N. Viltard, and P.-E. Kirstetter, 2013: A new methodology for rain identification from passive microwave data in the tropics using neural networks. *Quart. J. Roy. Meteor. Soc.*, **139**, 912–922, doi:10.1002/qj.2114.

Katsumata, M., H. Uyeda, K. Iwanami, and G. Liu, 2000: The response of 36-and 89-GHz microwave channels to convective snow clouds over ocean: Observation and modeling. *J. Appl. Meteor.*, **39**, 2322–2335, doi:10.1175/1520-0450(2000)039<2322:TROAGM>2.0.CO;2.

Kidd, C., D. Kniveton, and E. Barrett, 1998: The advantages and disadvantages of statistically derived–empirically calibrated passive microwave algorithms for rainfall estimation. *J. Atmos. Sci.*, **55**, 1576–1582, doi:10.1175/1520-0469(1998)055<1576:TAADOS>2.0.CO;2.

Kim, M.-J., J. Weinman, W. Olson, D.-E. Chang, G. Skofronick-Jackson, and J. Wang, 2008: A physical model to estimate snowfall over land using AMSU-B observations. *J. Geophys. Res.*, **113**, D09201, doi:10.1029/2007JD008589.

Kongoli, C., P. Pellegrino, R. R. Ferraro, N. C. Grody, and H. Meng, 2003: A new snowfall detection algorithm over land using measurements from the Advanced Microwave Sounding Unit (AMSU). *Geophys. Res. Lett.*, **30**, 1756, doi:10.1029/2003GL017177.

——, H. Meng, J. Dong, and R. Ferraro, 2015: A snowfall detection algorithm over land utilizing high-frequency passive microwave measurements—Application to ATMS. *J. Geophys. Res. Atmos.*, **120**, 1918–1932, doi:10.1002/2014JD022427.

Kulie, M. S., and R. Bennartz, 2009: Utilizing spaceborne radars to retrieve dry snowfall. *J. Appl. Meteor. Climatol.*, **48**, 2564–2580, doi:10.1175/2009JAMC2193.1.

——, ——, T. J. Greenwald, Y. Chen, and F. Weng, 2010: Uncertainties in microwave properties of frozen precipitation: Implications for remote sensing and data assimilation. *J. Atmos. Sci.*, **67**, 3471–3487, doi:10.1175/2010JAS3520.1.

——, L. Milani, N. B. Wood, S. A. Tushaus, R. Bennartz, and T. S. L. Ecuyer, 2016: A shallow cumuliform snowfall census using spaceborne radar. *J. Hydrometeor.*, **17**, 1261–1279, doi:10.1175/JHM-D-15-0123.1.

Kummerow, C. D., and L. Giglio, 1994: A passive microwave technique for estimating rainfall and vertical structure information from space. Part I: Algorithm description. *J. Appl. Meteor.*, **33**, 3–18, doi:10.1175/1520-0450(1994)033<0003:APMTFE>2.0.CO;2.

——, S. Ringerud, J. Crook, D. Randel, and W. Berg, 2011: An observationally generated a priori database for microwave rainfall retrievals. *J. Atmos. Oceanic Technol.*, **28**, 113–130, doi:10.1175/2010JTECHA1468.1.

——, D. L. Randel, M. Kulie, N.-Y. Wang, R. Ferraro, S. J. Munchak, and V. Petkovic, 2015: The evolution of the Goddard profiling algorithm to a fully parametric scheme. *J. Atmos. Oceanic Technol.*, **32**, 2265–2280, doi:10.1175/JTECH-D-15-0039.1.

Laviola, S., and V. Levizzani, 2011: The 183-WSL fast rain rate retrieval algorithm: Part I: Retrieval design. *Atmos. Res.*, **99**, 443–461, doi:10.1016/j.atmosres.2010.11.013.

Liu, G., 1998: A fast and accurate model for microwave radiance calculations. *J. Meteor. Soc. Japan*, **76** (2), 335–343.

——, 2008a: A database of microwave single-scattering properties for nonspherical ice particles. *Bull. Amer. Meteor. Soc.*, **89**, 1563–1570, doi:10.1175/2008BAMS2486.1.

——, 2008b: Deriving snow cloud characteristics from *CloudSat* observations. *J. Geophys. Res.*, **113**, D00A09, doi:10.1029/2007JD009766.

——, and J. A. Curry, 1997: Precipitation characteristics in Greenland–Iceland–Norwegian Seas determined by using satellite microwave data. *J. Geophys. Res.*, **102**, 13 987–13 997, doi:10.1029/96JD03090.

——, and E.-K. Seo, 2013: Detecting snowfall over land by satellite high-frequency microwave observations: The lack of scattering signature and a statistical approach. *J. Geophys. Res. Atmos.*, **118**, 1376–1387, doi:10.1002/jgrd.50172.

Löhnert, U., S. Kneifel, A. Battaglia, M. Hagen, L. Hirsch, and S. Crewell, 2011: A multisensor approach toward a better understanding of snowfall microphysics: The TOSCA project. *Bull. Amer. Meteor. Soc.*, **92**, 613–628, doi:10.1175/2010BAMS2909.1.

Mätzler, C., 1994: Passive microwave signatures of landscapes in winter. *Meteor. Atmos. Phys.*, **54**, 241–260, doi:10.1007/BF01030063.

Mejia, Y., H. Ghedira, S. Mahani, and R. Khanbilvardi, 2008: Robust neural network system design for detecting and estimating snowfall from the Advanced Microwave Sounding Unit. *J. Appl. Remote Sens.*, **2**, 023524, doi:10.1117/1.2953971.

Mugnai, A., and Coauthors, 2007: Snowfall measurements by proposed European GPM mission. *Measuring Precipitation from Space*, Advances in Global Change Research, Vol. 28, Springer, 655–674, doi:10.1007/978-1-4020-5835-6_49.

Munchak, S. J., and G. Skofronick-Jackson, 2013: Evaluation of precipitation detection over various surfaces from passive microwave imagers and sounders. *Atmos. Res.*, **131**, 81–94, doi:10.1016/j.atmosres.2012.10.011.

Noh, Y.-J., G. Liu, A. S. Jones, and T. H. Vonder Haar, 2009: Toward snowfall retrieval over land by combining satellite and in situ measurements. *J. Geophys. Res.*, **114**, D24205, doi:10.1029/2009JD012307.

Petty, G. W., 1995: The status of satellite-based rainfall estimation over land. *Remote Sens. Environ.*, **51**, 125–137, doi:10.1016/0034-4257(94)00070-4.

——, and W. Huang, 2010: Microwave backscatter and extinction by soft ice spheres and complex snow aggregates. *J. Atmos. Sci.*, **67**, 769–787, doi:10.1175/2009JAS3146.1.

Rienecker, M. M., and Coauthors, 2011: MERRA: NASA's Modern-Era Retrospective Analysis for Research and Applications. *J. Climate*, **24**, 3624–3648, doi:10.1175/JCLI-D-11-00015.1.

Seto, S., N. Takahashi, and T. Iguchi, 2005: Rain/no-rain classification methods for microwave radiometer observations over land using statistical information for brightness temperatures under no-rain conditions. *J. Appl. Meteor.*, **44**, 1243–1259, doi:10.1175/JAM2263.1.

——, T. Iguchi, and T. Oki, 2013: The basic performance of a precipitation retrieval algorithm for the Global Precipitation Measurement mission's single/dual-frequency radar measurements. *IEEE Trans. Geosci. Remote Sens.*, **51**, 5239–5251, doi:10.1109/TGRS.2012.2231686.

Shi, J., and Coauthors, 2010: WRF simulations of the 20–22 January 2007 snow events over eastern Canada: Comparison with in situ and satellite observations. *J. Appl. Meteor. Climatol.*, **49**, 2246–2266, doi:10.1175/2010JAMC2282.1.

Skofronick-Jackson, G., and B. T. Johnson, 2011: Surface and atmospheric contributions to passive microwave brightness temperatures for falling snow events. *J. Geophys. Res.*, **116**, D02213, doi:10.1029/2010JD014438.

——, M.-J. Kim, J. A. Weinman, and D.-E. Chang, 2004: A physical model to determine snowfall over land by microwave radiometry. *IEEE Trans. Geosci. Remote Sens.*, **42**, 1047–1058, doi:10.1109/TGRS.2004.825585.

——, B. T. Johnson, and S. J. Munchak, 2013: Detection thresholds of falling snow from satellite-borne active and passive sensors. *IEEE Trans. Geosci. Remote Sens.*, **51**, 4177–4189, doi:10.1109/TGRS.2012.2227763.

——, and Coauthors, 2015: Global Precipitation Measurement Cold Season Precipitation Experiment (GCPEX): For measurement's sake, let it snow. *Bull. Amer. Meteor. Soc.*, **96**, 1719–1741, doi:10.1175/BAMS-D-13-00262.1.

Smith, A., N. Lott, and R. Vose, 2011: The integrated surface database: Recent developments and partnerships. *Bull. Amer. Meteor. Soc.*, **92**, 704–708, doi:10.1175/2011BAMS3015.1.

Spencer, R. W., H. M. Goodman, and R. E. Hood, 1989: Precipitation retrieval over land and ocean with the SSM/I: Identification and characteristics of the scattering signal. *J. Atmos. Oceanic Technol.*, **6**, 254–273, doi:10.1175/1520-0426(1989)006<0254:PROLAO>2.0.CO;2.

Staelin, D. H., and F. W. Chen, 2000: Precipitation observations near 54 and 183 GHz using the *NOAA-15* satellite. *IEEE Trans. Geosci. Remote Sens.*, **38**, 2322–2332, doi:10.1109/36.868889.

Stephens, G. L., and C. D. Kummerow, 2007: The remote sensing of clouds and precipitation from space: A review. *J. Atmos. Sci.*, **64**, 3742–3765, doi:10.1175/2006JAS2375.1.

Surussavadee, C., and D. H. Staelin, 2009: Satellite retrievals of arctic and equatorial rain and snowfall rates using millimeter wavelengths. *IEEE Trans. Geosci. Remote Sens.*, **47**, 3697–3707, doi:10.1109/TGRS.2009.2029093.

Turk, F. J., Z. S. Haddad, and Y. You, 2014: Principal components of multifrequency microwave land surface emissivities. Part I: Estimation under clear and precipitating conditions. *J. Hydrometeor.*, **15**, 3–19, doi:10.1175/JHM-D-13-08.1.

Wang, N.-Y., C. Liu, R. Ferraro, D. Wolff, E. Zipser, and C. Kummerow, 2009: TRMM 2A12 land precipitation product—Status and future plans. *J. Meteor. Soc. Japan*, **87A**, 237–253, doi:10.2151/jmsj.87A.237.

Wang, Y., G. Liu, E.-K. Seo, and Y. Fu, 2013: Liquid water in snowing clouds: Implications for satellite remote sensing of snowfall. *Atmos. Res.*, **131**, 60–72, doi:10.1016/j.atmosres.2012.06.008.

Wilks, D. S., 2011: *Statistical Methods in the Atmospheric Sciences*. 3rd ed. International Geophysics Series, Vol. 100, Academic Press, 704 pp.

Xie, X., U. Löhnert, S. Kneifel, and S. Crewell, 2012: Snow particle orientation observed by ground-based microwave radiometry. *J. Geophys. Res.*, **117**, D02206, doi:10.1029/2011JD016369.

You, Y., and G. Liu, 2012: The relationship between surface rainrate and water paths and its implications to satellite rainrate retrieval. *J. Geophys. Res.*, **117**, D13207, doi:10.1029/2012JD017662.

——, ——, Y. Wang, and J. Cao, 2011: On the sensitivity of Tropical Rainfall Measuring Mission (TRMM) Microwave Imager channels to overland rainfall. *J. Geophys. Res.*, **116**, D12203, doi:10.1029/2010JD015345.

——, F. J. Turk, Z. S. Haddad, L. Li, and G. Liu, 2014: Principal components of multifrequency microwave land surface emissivities. Part II: Effects of previous-time precipitation. *J. Hydrometeor.*, **15**, 20–37, doi:10.1175/JHM-D-13-07.1.

——, N.-Y. Wang, and R. Ferraro, 2015: A prototype precipitation retrieval algorithm over land using passive microwave observations stratified by surface condition and precipitation vertical structure. *J. Geophys. Res. Atmos.*, **120**, 5295–5315, doi:10.1002/2014JD022534.

——, ——, ——, and P. Meyers, 2016: A prototype precipitation retrieval algorithm over land for ATMS. *J. Hydrometeor.*, **17**, 1601–1621, doi:10.1175/JHM-D-15-0163.1.